Fife organizes synaptic vesicles and calcium channels for high-probability neurotransmitter release

Joseph J. Bruckner,[1] Hong Zhan,[2] Scott J. Gratz,[2] Monica Rao,[1] Fiona Ukken,[2] Gregory Zilberg,[2] and Kate M. O'Connor-Giles[1,2,3]

[1]Cell and Molecular Biology Training Program, [2]Laboratory of Cell and Molecular Biology, and [3]Laboratory of Genetics, University of Wisconsin-Madison, Madison, WI 53706

The strength of synaptic connections varies significantly and is a key determinant of communication within neural circuits. Mechanistic insight into presynaptic factors that establish and modulate neurotransmitter release properties is crucial to understanding synapse strength, circuit function, and neural plasticity. We previously identified *Drosophila* Piccolo-RIM-related Fife, which regulates neurotransmission and motor behavior through an unknown mechanism. Here, we demonstrate that Fife localizes and interacts with RIM at the active zone cytomatrix to promote neurotransmitter release. Loss of Fife results in the severe disruption of active zone cytomatrix architecture and molecular organization. Through electron tomographic and electrophysiological studies, we find a decrease in the accumulation of release-ready synaptic vesicles and their release probability caused by impaired coupling to Ca^{2+} channels. Finally, we find that Fife is essential for the homeostatic modulation of neurotransmission. We propose that Fife organizes active zones to create synaptic vesicle release sites within nanometer distance of Ca^{2+} channel clusters for reliable and modifiable neurotransmitter release.

Introduction

The strength of synaptic transmission is a critical determinant of information processing in neural circuits. Evoked neurotransmission depends on localized Ca^{2+} influx triggering neurotransmitter release from synaptic vesicles at specialized domains of presynaptic terminals called active zones. At the active zone membrane, synaptic vesicles are docked and molecularly primed to respond to a rise in Ca^{2+} concentration by fusing with the membrane to release neurotransmitter. A conserved complex of active zone–associated proteins makes up the active zone cytomatrix (Ackermann et al., 2015). In *Drosophila melanogaster*, these proteins include the ELKS family protein Bruchpilot, Rab3-interacting molecule (RIM), RIM-binding protein, Unc13, and Fife (Aravamudan et al., 1999; Wang and Südhof, 2003; Wagh et al., 2006; Mittelstaedt and Schoch, 2007; Liu et al., 2011; Bruckner et al., 2012; Graf et al., 2012; Müller et al., 2012; Böhme et al., 2016). Active zone cytomatrix proteins contain many lipid- and protein-binding domains that mediate diverse interactions with key players in synaptic transmission, leading to the model that the active zone cytomatrix spatially organizes presynaptic terminals for the millisecond coupling of neurotransmitter release to action potentials.

The specific neurotransmitter release properties of an active zone are determined by two key parameters acting in concert: (1) the number of synaptic vesicles docked at the membrane and molecularly primed for Ca^{2+}-triggered release, termed the readily releasable pool, and (2) the release probability of these vesicles. Vesicle release probability is established by multiple parameters, including Ca^{2+} channel levels, localization and function at active zones, the spatial coupling of Ca^{2+} channels and release-ready vesicles, and the intrinsic Ca^{2+} sensitivity of individual vesicles. The observation that the presynaptic parameters of synaptic strength vary significantly even between the synapses of an individual neuron indicates that neurotransmitter release properties are determined locally at active zones and raises the question of how this complex regulation is achieved (Rosenmund et al., 1993; Murthy et al., 1997; Guerrero et al., 2005; Ariel et al., 2013; Melom et al., 2013). Genetic studies in *Drosophila*, *Caenorhabditis elegans*, and mice are revealing a key role for the active zone cytomatrix in determining the functional parameters underlying synaptic strength (Ackermann et al., 2015; Michel et al., 2015). A mechanistic understanding of how the active zone cytomatrix achieves local control of synaptic release properties will yield fundamental insights into neural circuit function.

We previously identified Fife, a Piccolo-RIM–related protein that is required for proper neurotransmitter release and motor behavior (Bruckner et al., 2012). Here, we demonstrate that Fife localizes to the active zone cytomatrix, where

Correspondence to Kate M. O'Connor-Giles: oconnorgiles@wisc.edu

Abbreviations used: EJC, excitatory junction current; EJP, excitatory junction potential; HPF/FS, high-pressure freeze/freeze substitution; mEJP, miniature EJP; NMJ, neuromuscular junction; RIM, Rab3-interacting molecule; SIM, structured illumination microscopy.

© 2017 Bruckner et al. This article is distributed under the terms of an Attribution–Noncommercial–Share Alike–No Mirror Sites license for the first six months after the publication date (see http://www.rupress.org/terms/). After six months it is available under a Creative Commons License (Attribution–Noncommercial–Share Alike 4.0 International license, as described at https://creativecommons.org/licenses/by-nc-sa/4.0/).

The Rockefeller University Press $30.00
J. Cell Biol. Vol. 216 No. 1 231–246
https://doi.org/10.1083/jcb.201601098

THE JOURNAL OF CELL BIOLOGY

Downloaded from http://rupress.org/jcb/article-pdf/216/1/231/1597608/jcb_201601098.pdf by guest on 08 February 2026

it interacts with RIM to promote neurotransmitter release. The active zone cytomatrix is diminished and molecularly disorganized at *Fife* mutant synapses, and Fife is critical for vesicle docking at the active zone membrane. Not only are the number of release-ready vesicles reduced in the absence of Fife, but their probability of release is also significantly impaired because of disrupted coupling to calcium channels. These results suggest that Fife promotes high-probability neurotransmitter release by organizing the active zone cytomatrix to create vesicle release sites in nanometer proximity to clustered Ca^{2+} channels. Finally, we find that in addition to its role in determining baseline synaptic strength, Fife plays an essential role in presynaptic homeostatic plasticity. Together, these findings provide mechanistic insight into how synaptic strength is established and modified to tune communication in neural circuits.

Results

Fife physically and functionally interacts with RIM

Fife is composed of a zinc finger domain, a PDZ domain, and two C2 domains, which each display significant homology with these domains of the core vertebrate active zone cytomatrix proteins Piccolo, RIM1, and RIM2 (Fig. 1 A; Bruckner et al., 2012). RIM proteins regulate synaptic vesicle priming through physical interactions with Unc13 and vesicle–Ca^{2+} channel coupling through physical interactions with vesicular Rab3, Ca^{2+} channel–interacting RIM-binding protein, and synaptic Ca^{2+} channels themselves (Koushika et al., 2001; Hibino et al., 2002; Deng et al., 2011; Kaeser et al., 2011; Graf et al., 2012; Müller et al., 2012). We hypothesized that Fife might also function closely with RIM to regulate neurotransmitter release properties. To assess whether Fife and RIM physically interact, we conducted coimmunoprecipitation experiments between the four noncanonical C2 domains of Fife and RIM. Canonical C2 domains confer Ca^{2+}-dependent lipid binding through five conserved aspartate residues, whereas noncanonical C2 domains, lacking some or all of the Ca^{2+}-interacting aspartates, may mediate Ca^{2+}-independent lipid binding or protein–protein interactions (Cho and Stahelin, 2006). We found that both Fife C2 domains bind the C2B, but not the C2A, domain of RIM (Fig. 1 B and not depicted). Both interactions were also observed in reciprocal coimmunoprecipitation experiments, demonstrating that Fife and RIM physically interact through their conserved C2 domains (Fig. S1).

We next investigated whether Fife and RIM function together to regulate neurotransmitter release. A recent study found that neurotransmitter release is severely impaired in *RIM-binding protein*/+; *RIM*/+ double heterozygous animals, but not in either single heterozygote (Müller et al., 2015). Double heterozygous interactions are rare and indicate that two proteins function closely together to regulate the same process. We found that loss of one copy of either *RIM* (*RIM*/+) or *Fife* (*Fife*/+) left neurotransmitter release intact, allowing us to investigate double heterozygous interactions. In contrast to single heterozygotes, loss of one copy of each gene (*Fife*+/+*RIM*) leads to a reduction in neurotransmitter release as severe as *Fife* and *RIM* homozygotes (Fig. 1, C–H). Thus, consistent with their biochemical interaction, Fife and RIM function closely together to determine synaptic release properties.

Fife colocalizes with RIM at the active zone cytomatrix

We previously demonstrated that transgenically expressed full-length, N-terminally tagged Fife rescues *Fife* neurotransmitter release deficits and overlaps with the *Drosophila* ELKS-related protein Bruchpilot (Bruckner et al., 2012). Bruchpilot is a major molecular component of the active zone cytomatrix, which can be discerned as discrete punctate structures in confocal images of motoneuron boutons (Kittel et al., 2006; Wagh et al., 2006). Similarly, UAS-RIM::GFP rescues synaptic deficits in *RIM* mutants and colocalizes with Bruchpilot at the active zone cytomatrix (Graf et al., 2012). Multiple attempts to generate antibodies that recognize Fife or RIM have been unsuccessful, so we coexpressed FLAG::Fife and RIM::GFP in neurons to determine whether the two proteins overlap in vivo (Bruckner et al., 2012; Graf et al., 2012). As predicted by their physical and functional interactions, we observed extensive colocalization at active zones of the neuromuscular junction (NMJ; Fig. 2 A).

We next sought to visualize endogenous Fife at active zones using CRISPR-based genome engineering to introduce a fluorescent or peptide tag at sequences common to all three *Fife* isoforms. In agreement with our previous observations, endogenously tagged Fife was broadly expressed at central and peripheral synapses and exhibited extensive overlap with Bruchpilot (Fig. 2, B and C). At the ventral ganglion, we observed endogenously tagged Fife in cell bodies and throughout the synaptic neuropil (Fig. 2 B). In the periphery, our endogenously tagged lines exhibited variable expressivity at the cellular level, suggesting that Fife is sensitive to the addition of a tag. *Fife* lines engineered to express an HA tag immediately downstream of the PDZ domain showed the most consistent expression in motor axons and NMJs, where $Fife^{Int\text{-}HA}$ localized in a punctate pattern that significantly overlapped with Bruchpilot at the active zone cytomatrix (Fig. 2 C). Fife endogenously tagged with GFP at the N terminus ($Fife^{Nterm\text{-}GFP}$) exhibited the identical subcellular pattern, demonstrating that active zone localization is tag independent (Fig. 2 D). Thus, we conclude that Fife is an integral component of the active zone cytomatrix that regulates neurotransmitter release at least in part through conserved interactions with RIM.

Fife active zone cytomatrices are smaller and molecularly disorganized

The active zone cytomatrix of the *Drosophila* NMJ is readily observed in electron micrographs of conventional chemically fixed preparations as a T-shaped electron density, often referred to as a T-bar, projecting from the active zone membrane into the bouton interior. At the ultrastructural level, the conserved proteins of the active zone cytomatrix adopt distinct structures at different synapses both within and between species (Zhai and Bellen, 2004; Bruckner et al., 2015). These structural differences likely reflect the distinct functions and release properties of these synapses and imply an important relationship between cytomatrix structure and synaptic function.

To assess cytomatrix structure in *Fife* mutants, we turned to high-pressure freeze/freeze substitution (HPF/FS) electron microscopy, which enables the instant immobilization of intact larvae and preservation of cellular ultrastructure in near-native state. As has been observed in previous studies, the ultrastructure of the cytomatrix is resolved as a complex network of proteinaceous filaments in larvae prepared for electron microscopy via HPF/FS (Fig. 3 A; Fouquet et al., 2009; Jiao et al., 2010).

Downloaded from http://rupress.org/jcb/article-pdf/216/1/231/1597608/jcb_201601098.pdf by guest on 08 February 2026

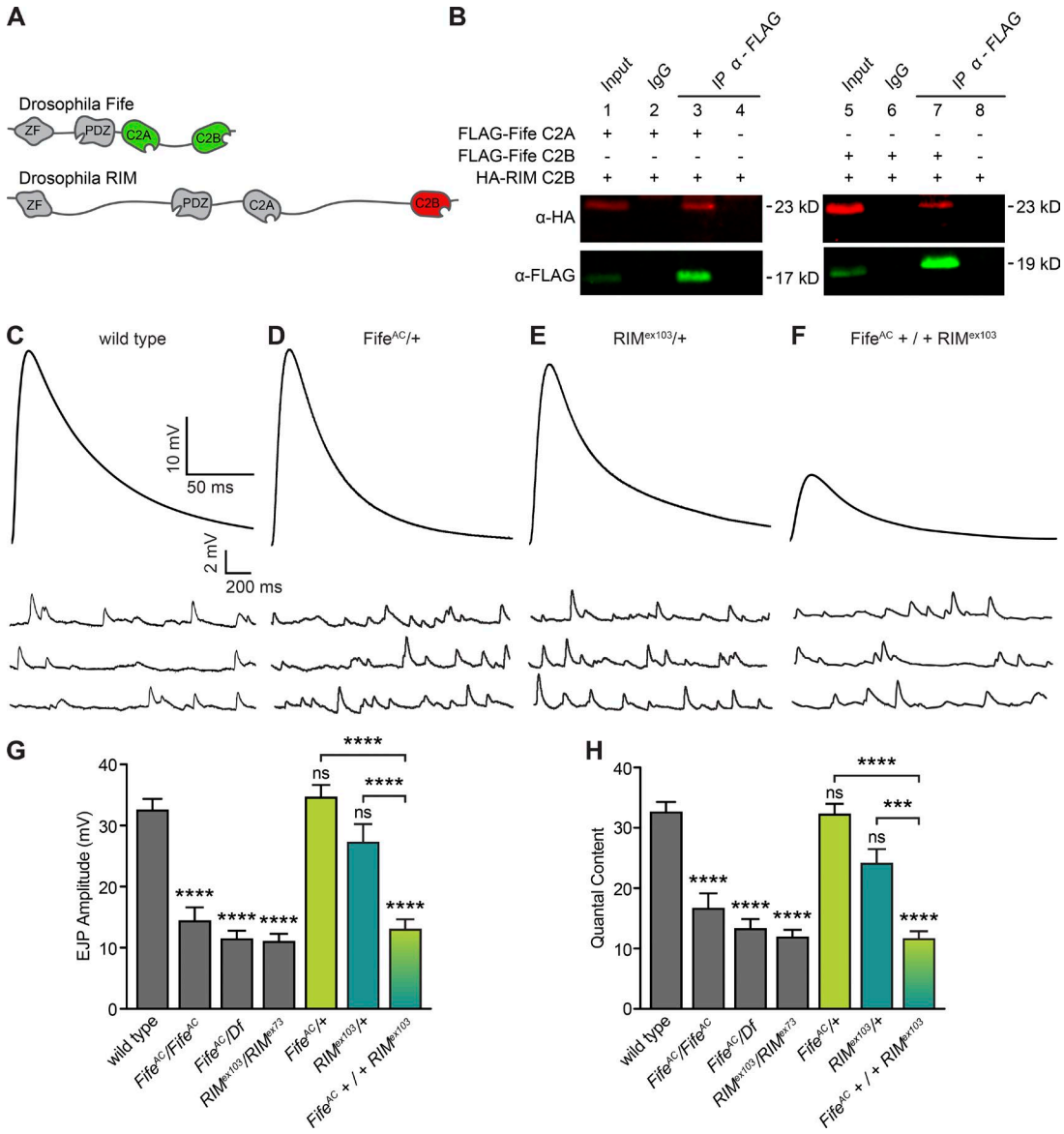

Figure 1. **Fife interacts with RIM.** (A) Fife and RIM domain structures, indicating the interacting Fife C2A and C2B (green) and RIM C2B (red) domains. (B) FLAG-tagged Fife C2A (green, lanes 1–4) and C2B (green, lanes 5–8) specifically precipitate HA-tagged RIM C2B (red). Input lanes contain lysate equal to 10% of the amount used for the pull-down assays. IP indicates the antibody used for immunoprecipitation. IgG bands at 25 kD are not depicted. (C–F) Representative traces of EJPs and mEJPs recorded in 0.6 mM Ca^{2+} at wild type (C), *Fife*^{AC}/+ (D), *RIM*^{ex103}/+ (E), and *Fife*^{AC}+/+*RIM*^{ex103} (F) NMJs. Stimulus artifacts have been removed for clarity. (G) Mean EJP amplitude is significantly reduced in *Fife*^{AC}/*Fife*^{AC}, *Fife*^{AC}/*Df*, *RIM*^{ex103}/*RIM*^{ex73}, and *Fife*^{AC}+/+*RIM*^{ex103}, but not in *Fife*^{AC}/+ or *RIM*^{ex103}/+ compared with wild type (wild type, 32.44 ± 1.90 mV, *n* = 7 NMJs; *Fife*^{AC}/*Fife*^{AC}, 14.32 ± 2.29 mV, *n* = 11 NMJs, P < 0.0001; *Fife*^{AC}/*Df*, 11.37 ± 1.40 mV, *n* = 15 NMJs, P < 0.0001; *RIM*^{ex103}/*RIM*^{ex73}, 10.93 ± 1.35 mV, *n* = 8 NMJs, P < 0.0001; *Fife*^{AC}/+, 34.54 ± 2.12 mV, *n* = 9 NMJs, P = 0.99; *RIM*^{ex103}/+, 27.19 ± 3.06 mV, *n* = 12 NMJs, P = 0.74; *Fife*^{AC}+/+*RIM*^{ex103}, 12.94 ± 1.68 mV, *n* = 12 NMJs, P < 0.0001). Mean EJP amplitude is also significantly reduced in *Fife*^{AC}+/+*RIM*^{ex103} compared with *Fife*^{AC}/+ (P < 0.0001) or *RIM*^{ex103}/+ (P < 0.0001). (H) Mean quantal content is also significantly reduced in *Fife*^{AC}/*Fife*^{AC}, *Fife*^{AC}/*Df*, *RIM*^{ex103}/*RIM*^{ex73}, and *Fife*^{AC}+/+*RIM*^{ex103}, but not in *Fife*^{AC}/+ or *RIM*^{ex103}/+ compared with wild type (wild type, 32.56 ± 1.74, *n* = 7 NMJs; *Fife*^{AC}/*Fife*^{AC}, 16.59 ± 2.56, *n* = 11 NMJs, P < 0.0001; *Fife*^{AC}/*Df*, 13.22 ± 1.65, *n* = 15 NMJs, P < 0.0001; *RIM*^{ex103}/*RIM*^{ex73}, 11.80 ± 1.33, *n* = 8 NMJs, P < 0.0001; *Fife*^{AC}/+, 32.18 ± 1.81, *n* = 9 NMJs, P = 0.99; *RIM*^{ex103}/+, 24.04 ± 2.44, *n* = 12 NMJs, P = 0.75; *Fife*^{AC}+/+*RIM*^{ex103}, 11.55 ± 1.35 mV, *n* = 12 NMJs, P < 0.0001). Mean quantal content is also significantly reduced in *Fife*^{AC}+/+*RIM*^{ex103} compared with *Fife*^{AC}/+ (P < 0.0001) or *RIM*^{ex103}/+ (P < 0.0001). ns, not significant; ***, P < 0.001, ****, P < 0.0001; analysis of variance followed by *post hoc* tests with Šidák correction. Error bars represent SEM.

We noted that the electron-dense cytomatrix appeared smaller at *Fife* NMJs (Fig. 3 B). To quantify cytomatrix size, we measured their maximum widths and found a nearly 25% reduction at *Fife* active zones (Fig. 3, A–C). We observed a similar reduction in T-bar size in micrographs of conventionally prepared *Fife*^{ex}/*Df* active zones (Fig. 3 D).

To determine whether the decreased cytomatrix size we observed at the ultrastructural level is reflected in alterations to the molecular organization of the cytomatrix, we used structured illumination microscopy (SIM) to visualize Bruchpilot localization. In contrast to the highly ordered, ring-shaped pattern observed at wild-type active zones, Bruchpilot rarely displays a clear ring structure in *Fife* mutants (Fig. 3, E and F; Kittel et al., 2006). To quantify this difference, we assessed the distribution of Bruchpilot at wild-type and *Fife* mutant active zones by plotting a fluorescence intensity profile along a line drawn

Downloaded from http://rupress.org/jcb/article-pdf/216/1/231/1597608/jcb_201601098.pdf by guest on 08 February 2026

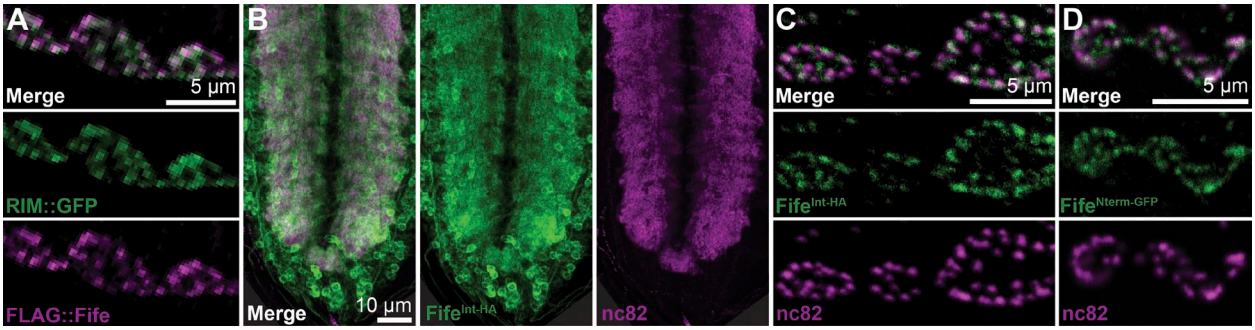

Figure 2. **Fife localizes to the active zone cytomatrix.** (A) Single optical section (0.4 µm) of *C155-Gal4/Y; UAS-RIM-GFP/+; UAS-FLAG-Fife/+* NMJ boutons colabeled with antibodies against GFP (green) and FLAG (purple). (B) Single optical section (1.2 µm) of a larval ventral ganglion homozygous for Fife endogenously tagged at an internal site common to all isoforms ($Fife^{Int\text{-}HA}$) and colabeled with antibodies against HA (green) and Bruchpilot (nc82, purple). (C) Single optical section (0.1 µm) of NMJ boutons homozygous for the same internal endogenous tag as in B and colabeled with antibodies against HA (green) and Bruchpilot (purple). (D) Single optical section (0.4 µm) of NMJ boutons homozygous for Fife endogenously tagged at the N-terminus ($Fife^{Nterm\text{-}GFP}$) and colabeled with antibodies against HA (green) and Bruchpilot (nc82, purple).

through the center of each planar-oriented Bruchpilot spot. The mean intensity profile of Bruchpilot spots in *Fife* mutants revealed the loss of the two-peak profile associated with the ring structure observed in wild type (Fig. 3, G and H). In *Fife* mutants, we measured 70% fewer active zones with two peaks than in wild type, indicating severe disruption of active zone organization (Fig. 3 I).

Fife regulates synaptic probability of release

Recent studies have revealed a correlation between the size and molecular composition of the active zone cytomatrix and synaptic release probability in diverse neuronal subtypes (Branco et al., 2010; Hallermann et al., 2010c; Matz et al., 2010; Peled and Isacoff, 2011; Weyhersmüller et al., 2011; Holderith et al., 2012; Matkovic et al., 2013; Ehmann et al., 2014). We previously found that evoked neurotransmitter release is significantly decreased in the absence of Fife, whereas active zone number is normal, suggesting impaired release probability at *Fife* synapses. In support of this possibility, we found that upon stimulation in low extracellular Ca^{2+} concentrations, *Fife* NMJs fail to release neurotransmitter significantly more frequently than control NMJs (Fig. 4 A). Additionally, paired-pulse facilitation experiments showed that in response to paired stimuli at 20 Hz in 0.6 mM external Ca^{2+}, wild-type NMJs exhibited almost no facilitation (Fig. 4, B–D). In contrast, *Fife* NMJs exhibited an ∼60% increase in excitatory junction potential (EJP) amplitude (Fig. 4, B–D). Together, these data indicate that Fife NMJs have an impaired synaptic probability of release.

Fife regulates the size of the readily releasable pool of synaptic vesicles

A key determinant of synaptic probability of release is the number of vesicles at the active zone membrane primed for Ca^{2+}-dependent release. To obtain physiological estimates of the size of this readily releasable pool of vesicles, multiple studies have used high-frequency stimulus trains that result in short-term synaptic depression caused by depletion of release-ready vesicles (Schneggenburger et al., 1999; Hallermann et al., 2010b; Miśkiewicz et al., 2011; Weyhersmüller et al., 2011). After depletion, a steady state of release representing the immediate release of vesicles trafficked from the recycling pool is observed, enabling back extrapolation of readily releasable pool size. To assess *Fife*'s role in determining the number of release-ready synaptic vesicles, we measured the amplitude of postsynaptic responses during 60-Hz stimulus trains in 1 mM $[Ca^{2+}]_e$. We then determined the amount of neurotransmitter release (quantal content) for each response and plotted cumulative quantal content (Fig. 5 A). By fitting a line to the last 10 of 30 cumulative quantal content measurements for each NMJ and back extrapolating to time zero, we calculated the mean readily releasable vesicle pool size at wild-type and *Fife* active zones and found that the number of release-ready vesicles at *Fife* NMJs is decreased by ∼40% (Fig. 5 B).

The readily releasable pool of vesicles can also be assessed morphologically in electron micrographs, where it is thought to correlate with those vesicles closely associated with the active zone membrane (Rizzoli and Betz, 2005; Alabi and Tsien, 2012; Neher, 2015). To complement our electrophysiological estimates, we quantified synaptic vesicles within 5 nm of the active zone membrane in ultrathin sections of wild-type and *Fife* synapses preserved using HPF/FS to avoid alteration of vesicle-membrane associations induced by conventional chemical preservation (Siksou et al., 2009). We observed a similar 30% decrease in membrane-associated vesicles at *Fife* active zones (Fig. 5, C–E). Thus, morphological analysis of *Fife* NMJs supports the electrophysiological finding that Fife promotes the accumulation of release-ready synaptic vesicles.

Fife promotes synaptic vesicle docking

To gain spatial insight into the relationship between active zone cytomatrix structure and the regulation of the readily releasable vesicle pool, we expanded our analysis to electron tomography of HPF/FS-prepared samples. Tomographic reconstruction of each active zone in 250-nm sections coupled with semiautomatic segmentation of membrane and protein structures allows us to build highly detailed 3D models of active zone structure (Videos 1 and 2; see Materials and Methods). The active zone cytomatrix, comprising a complex proteinaceous network that becomes less dense with distance from both the membrane and the active zone center, is vividly revealed in both virtual sections and 3D models of segmented tomograms (Fig. 6, A and B; and Videos 1 and 2, blue structure). Synaptic vesicles cluster broadly around the active zone cytomatrix (Fig. 6, A and B, colored spheres). As has been observed in mammalian central synapses and *C. elegans* and zebrafish NMJs, we found that the majority of synaptic vesicles are linked to one another in a network of fine structures,

Downloaded from http://rupress.org/jcb/article-pdf/216/1/231/1597608/jcb_201601098.pdf by guest on 08 February 2026

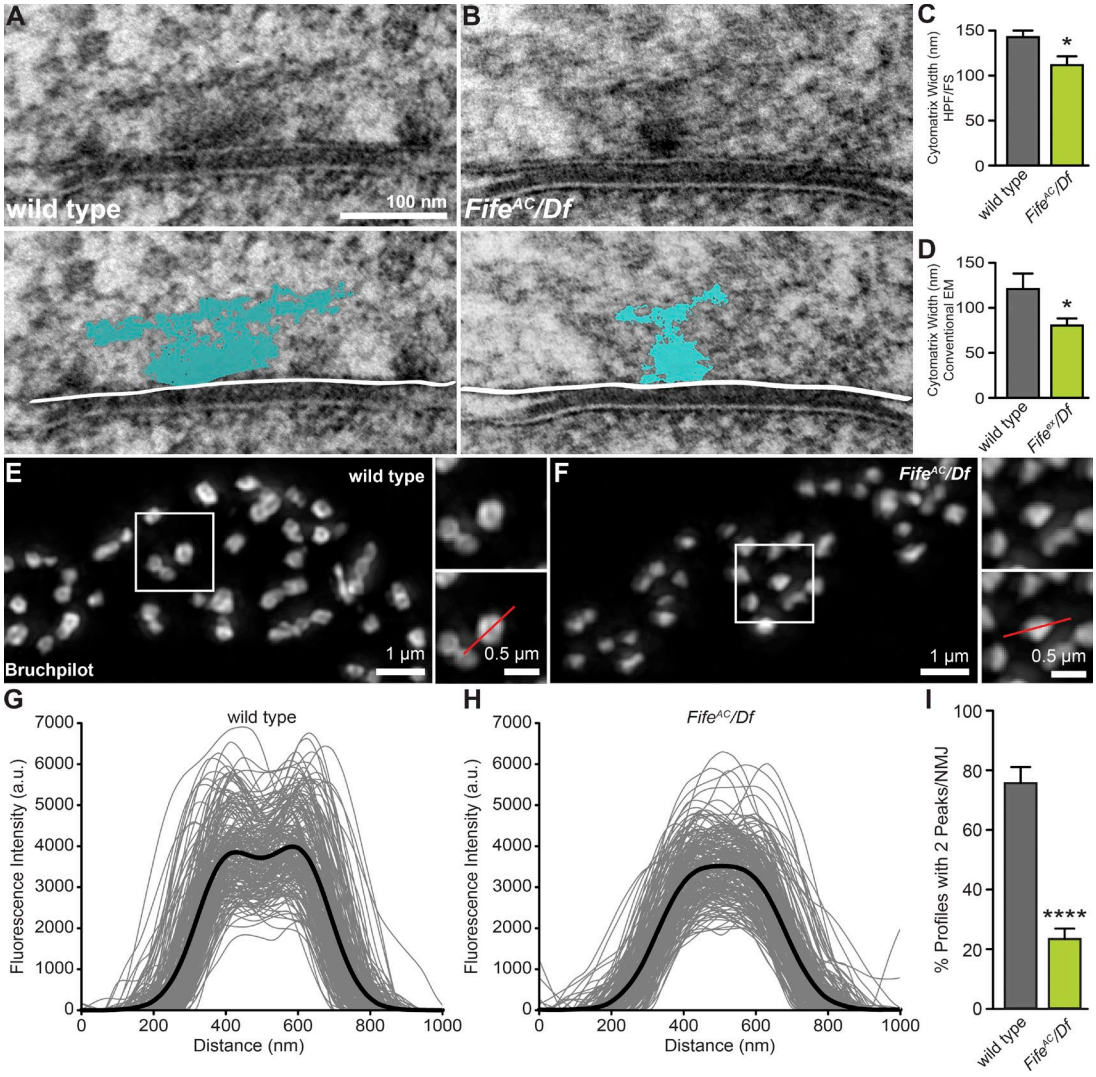

Figure 3. **Fife regulates active zone size and molecular organization.** (A–D) Reduced active zone cytomatrix size in electron micrographs of ultrathin sections of wild-type (A) and *Fife* (B) NMJs. The width of the cytomatrix (blue) in samples prepared using HPF/FS techniques (A–C) is significantly reduced in $Fife^{AC}/Df$ (111.0 ± 9.6 nm, n = 31 cytomatrices) compared with wild type (141.9 ± 7.3 nm, n = 46 cytomatrices, P = 0.011). A similar reduction is observed between $Fife^{ex}/Df$ (80.4 ± 7.8 nm, n = 17 cytomatrices) and wild-type (121.0 ± 17.1 nm, n = 13 cytomatrices, P = 0.046) cytomatrices in aldehyde-fixed samples (D). (E and F) SIM images of wild-type (E) and $Fife^{AC}/Df$ (F) NMJs stained with nc82 anti-Bruchpilot antibody. Insets in E and F show representative Bruchpilot punctae and an example line scan used to generate intensity profiles (red line). (G and H) Fluorescence intensity profiles along a line bisecting individual Bruchpilot punctae (gray lines) and the mean intensity profiles (black lines) are shown for wild type (G, n = 198 active zones) and $Fife^{AC}/Df$ (H, n = 200 active zones). (I) Quantification of the percentage of plot profiles with two peaks per wild type (75.7 ± 5.4%, n = 10 NMJs [198 active zones]) and $Fife^{AC}/Df$ (23.4 ± 3.5%, n = 10 NMJs [200 active zones]; P < 0.0001) NMJ. *, P < 0.05, ****, P < 0.0001, Student's t test. Error bars represent SEM.

termed connectors, that are preserved in HPF/FS-preserved specimens (Fig. 6, B and C, green filaments; Landis et al., 1988; Rostaing et al., 2006; Fernández-Busnadiego et al., 2010; Stigloher et al., 2011; Leitinger et al., 2012; Helmprobst et al., 2015; Zhan et al., 2016). Synaptic vesicles are also tethered to or docked at the active zone membrane (Fig. 6, A and B, gold and olive spheres, respectively). A subset of docked vesicles are also in direct contact with the active zone cytomatrix (Fig. 6, A and B, magenta spheres).

We next applied electron tomography to HPF/FS-prepared *Fife* mutants to visualize the organization of the active zone cytomatrix and membrane-associated vesicles thought to represent the release-ready vesicle pool. Consistent with our thin-section electron microscopy and SIM results, the electron-dense cytomatrix appears smaller and less complex in the absence of *Fife* (Fig. 6, C and D). Vesicles linked to the membrane by tethers of varying length and vesicles in direct morphological contact with the presynaptic membrane are clearly observed in our tomograms (Fig. 6, E–H). It has been proposed that future release-ready vesicles are first anchored to the active zone membrane by a single long tether, followed by tight membrane association and the accumulation of multiple short connections to the membrane proposed to be priming factors (Siksou et al., 2009; Fernández-Busnadiego et al., 2010; Hallermann and Silver, 2013). Our tomograms suggest that between these steps, vesicles accumulate additional long tethers, which we define as >5 nm, as they move closer to the membrane (Fig. 6, E and F). At wild-type active zones, vesicles with a single membrane tether are a mean of 30.2 nm from the membrane, whereas vesicles with more than one long tether reside a mean of 20.1 nm

Downloaded from http://rupress.org/jcb/article-pdf/216/1/231/1597608/jcb_201601098.pdf by guest on 08 February 2026

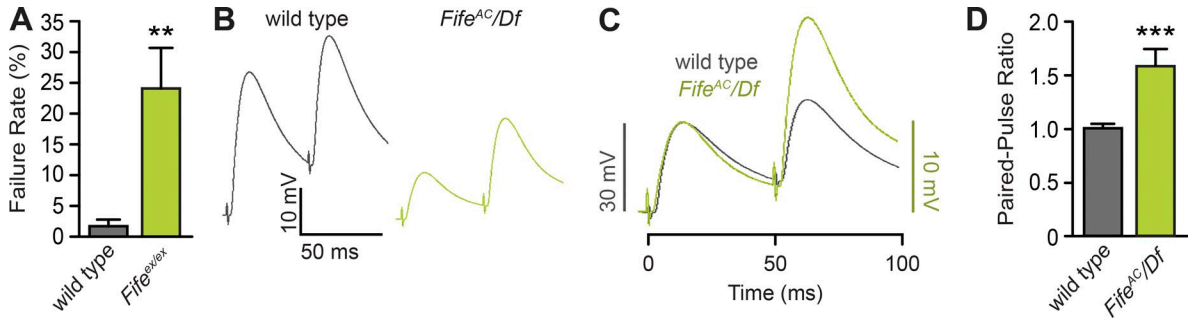

Figure 4. **Fife regulates synaptic probability of release.** (A) In 0.2 mM Ca^{2+}, *Fife* NMJs fail to respond to a presynaptic stimulus significantly more frequently than wild type (wild type: 1.8 ± 1.1%, n = 6 NMJs vs. $Fife^{ex/ex}$: 24.1 ± 6.6%, n = 11 NMJs; P = 0.007). (B) Representative traces of paired EJPs in wild type and $Fife^{AC}/Df$ recorded in 0.6 mM Ca^{2+}. (C and D) In 0.6 mM Ca^{2+}, *Fife* NMJs facilitate significantly in response to paired pulses delivered at 20 Hz, as illustrated by representative traces scaled to the amplitude of the first wild-type pulse (C) and mean ratio of the amplitude of the first and second responses (D; wild type: 1.01 ± 0.04, n = 10 NMJs vs. $Fife^{AC}/Df$: 1.58 ± 0.16, n = 14 NMJs, P = 0.0004). The scale of EJPs in C is indicated by the black bar on the left for wild type and green bar on the right for $Fife^{AC}/Df$. **, P < 0.01; ***, P < 0.001; Mann–Whitney U test. Error bars represent SEM.

from the membrane (Fig. 6, E and F; 30.2 ± 2.8 nm, n = 29 vesicles with one tether, vs. 20.1 ± 1.5 nm, n = 48 vesicles with more than one tether, in 16 wild-type tomograms; P = 0.006). To assess where Fife functions in establishing the readily releasable pool of vesicles, we first quantified the number of synaptic vesicles attached to the membrane by one or more long tethers and observed no difference between wild type and *Fife* (Fig. 6, E, F, and I). Similarly, the length of tethers was unaffected in *Fife* mutants (unpublished data). We next assessed those vesicles in direct contact with the active zone membrane by focusing exclusively on our highest resolution double-tilt tomograms, where vesicles directly contacting the membrane could be unambiguously distinguished from those in close proximity (Videos 1 and 3). In both genotypes, the majority of membrane-docked vesicles had multiple short connections to the membranes discernable in at least one virtual section (Fig. 6, G and H; wild type, 66%; $Fife^{AC}/Df$, 67%). Consistent with severe depletion of the readily releasable vesicle pool, there were 52% fewer docked vesicles at *Fife* active zones (Fig. 6, G, H, and J). The number of docked vesicles declined with distance from the cytomatrix, with the great majority residing within 150 nm of the cytomatrix center (Fig. 6 K). In *Fife* mutants, we observed a clear trend toward fewer cytomatrix-associated docked vesicles, with a mean of 0.9 per *Fife* synapse compared with 1.7 per wild-type synapse (Fig. 6 L). Together, these data indicate that Fife promotes membrane docking to establish the readily releasable vesicle pool and suggest that Fife may facilitate the interaction of docked vesicles with the active zone cytomatrix.

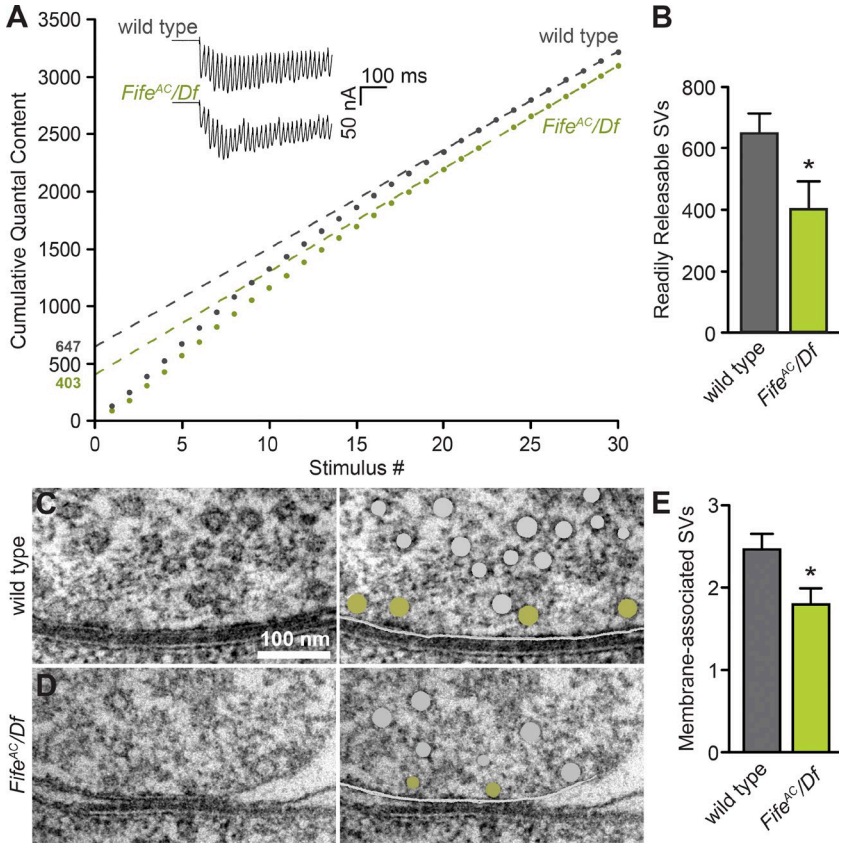

Figure 5. **Fife regulates the readily releasable pool of synaptic vesicles.** (A and B) Representative traces of EJCs and mean cumulative quantal content (A) in wild type (gray) and $Fife^{AC}/Df$ (green) during 60-Hz stimulus trains in 1 mM $[Ca^{2+}]_e$. Mean readily releasable vesicle pool size (B) estimated by back extrapolation of a line fitted to the last 10 of 30 cumulative quantal content measurements is significantly reduced in $Fife^{AC}/Df$ (403 ± 88 vesicles, n = 6 NMJs) compared with wild type (647 ± 67 vesicles, n = 9 NMJs, P = 0.043). (C–E) Representative electron micrographs of ultrathin sections of wild-type (C) and $Fife^{AC}/Df$ (D) active zones prepared by HPF/FS. Active zone–associated synaptic vesicles are colored gray (C and D, right panels), vesicles in direct contact with or tethered within 5 nm of the presynaptic membrane (marked in white) were quantified and are colored green (C and D, right). (E) Mean number of membrane-associated vesicles at $Fife^{AC}/Df$ active zones (1.8 ± 0.19 vesicles, n = 30 active zones) is significantly reduced compared with wild-type (2.5 ± 0.19 vesicles, n = 30 active zones, P = 0.017). *, P < 0.05, Student's t test. Error bars represent SEM.

Downloaded from http://rupress.org/jcb/article-pdf/216/1/231/1597608/jcb_201601098.pdf by guest on 08 February 2026

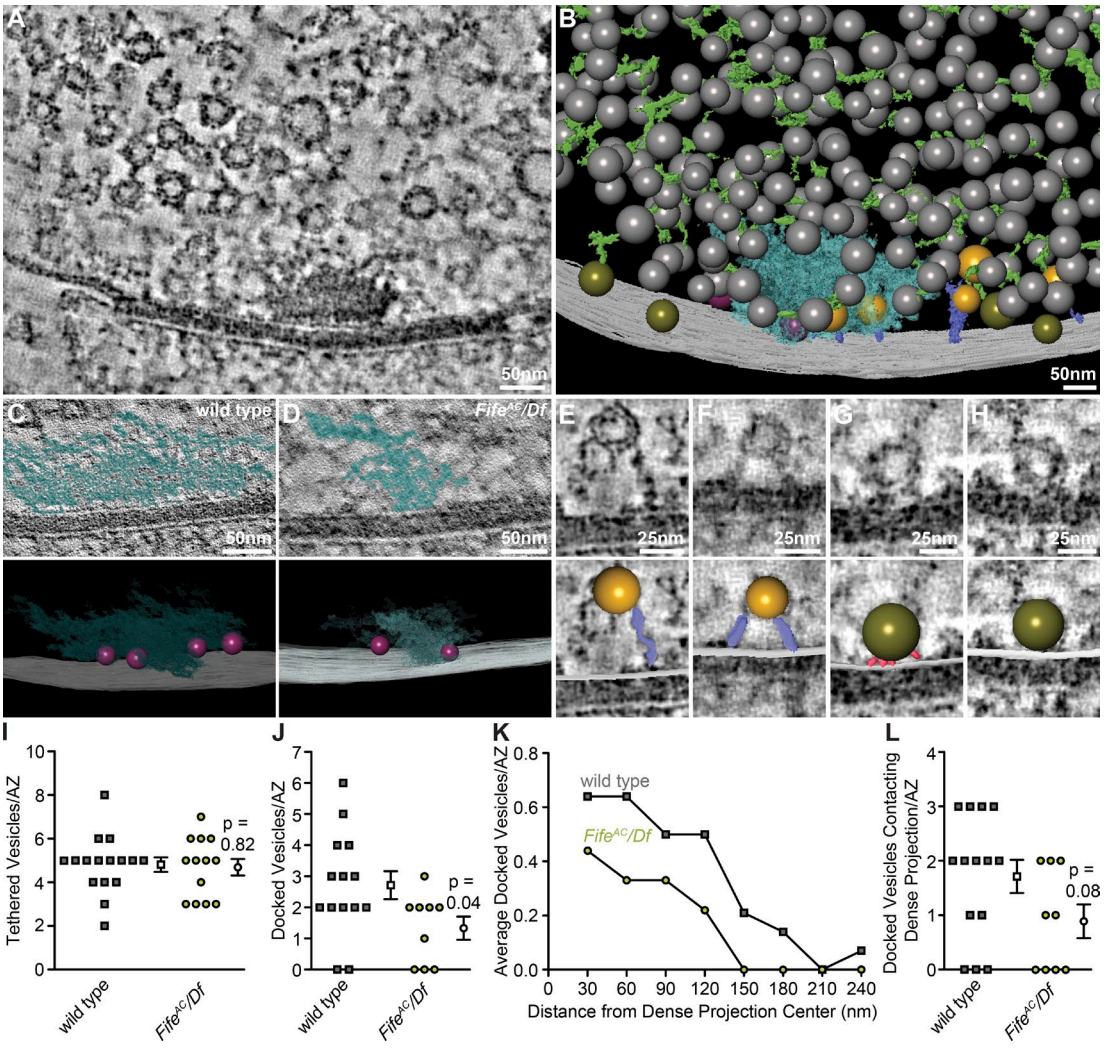

Figure 6. **Fife promotes synaptic vesicle docking.** (A) Single, central virtual slice of ∼0.7 nm through an EM tomogram of a wild-type NMJ synapse. (B) 3D model of an extensively segmented wild-type active zone prepared using HPF/FS techniques, illustrating the cytomatrix (blue) and synaptic vesicles (clustered pool in gray, tethered vesicles in gold, release-ready vesicles in contact with the cytomatrix in magenta, and release-ready vesicles distal to the cytomatrix in olive), tethers linking synaptic vesicles to the presynaptic membrane (purple), and connectors linking synaptic vesicles within the clustered pool (green). (C–D) Representative virtual slices with segmented cytomatrices superimposed (top) and 3D models (bottom) of cytomatrices (blue) and membrane-associated synaptic vesicles (magenta) at representative wild-type (C) and *Fife*^{AC}*/Df* (D) active zones. (E–F) Virtual slices of ∼0.7 nm from wild-type tomograms (E and F) and the same virtual slices with 3D models of segmented features superimposed (bottom) of representative tethered synaptic vesicles (gold) linked to the presynaptic membrane by single (E) or multiple (F) long filaments (purple). (G–H) Virtual slices from wild-type tomograms and the same virtual slices with 3D models of segmented features superimposed (bottom) of representative docked synaptic vesicles (olive) with (G) or without (H) numerous short connections (red) between the vesicle and presynaptic membranes. (I) Quantification of the number of synaptic vesicles per active zone tethered by long filaments (gold vesicles) in wild type (4.8 ± 1.3 vesicles per active zone, *n* = 16 active zones) and *Fife*^{AC}*/Df* (4.7 ± 1.4 vesicles per active zone, *n* = 13 active zones P = 0.81). (J) Quantification of the number of synaptic vesicles per active zone docked at the presynaptic membrane (magenta and olive vesicles) in wild type (2.7 ± 0.45 vesicles, *n* = 14 active zones) and *Fife*^{AC}*/Df* (1.3 ± 0.37 vesicles, *n* = 9 active zones P = 0.04). (K) Histogram of the mean number of docked synaptic vesicles, in 30-nm bins, at indicated distances from the dense projection center in wild type (*n* = 38 docked vesicles at 14 active zones) and *Fife*^{AC}*/Df* (*n* = 12 docked vesicles at nine active zones). (L) Quantification of the number of docked synaptic vesicles per active zone in contact with the dense projection (magenta vesicles) in wild type (1.7 ± 0.30 vesicles, *n* = 14 active zones) and *Fife*^{AC}*/Df* (0.9 ± 0.31 vesicles, *n* = 9 active zones P = 0.08). Student's *t* test. Error bars represent SEM.

Fife promotes synaptic vesicle-Ca^{2+} channel coupling

In addition to the number of release-ready vesicles at an active zone, their individual probability of release is a key factor in determining synaptic strength. Local increases in Ca^{2+} levels surrounding voltage-dependent Ca^{2+} channels promote the fusion of release-ready vesicles. Thus, key parameters in determining vesicular release probabilities are Ca^{2+} channel levels and the physical distance between Ca^{2+} channels and release-ready vesicles (Brandt et al., 2005; Sakaba et al., 2005; Schlüter et al., 2006; Wadel et al., 2007; Bucurenciu et al., 2010; Weber et al., 2010; Lee et al., 2013; Schmidt et al., 2013; Ishiyama et al., 2014; Chen et al., 2015; Nakamura et al., 2015; Stanley, 2015).

At the *Drosophila* NMJ, GFP-tagged Cacophony, the pore-forming subunit of the *Drosophila* Ca_V2-type Ca^{2+} channel, clusters beneath the active zone cytomatrix (Kawasaki et al., 2002). To investigate whether the smaller, disordered cytomatrix of *Fife* active zones clusters fewer Ca^{2+} channels, we expressed GFP-Cacophony in wild-type and *Fife*^{AC}*/Df* motoneurons. We measured Cacophony levels relative to the neuronal membrane marker HRP and found a 13% decrease in Cacophony intensity, indicating a mild impairment (Fig. 7, A–C). We

Downloaded from http://rupress.org/jcb/article-pdf/216/1/231/1597608/jcb_201601098.pdf by guest on 08 February 2026

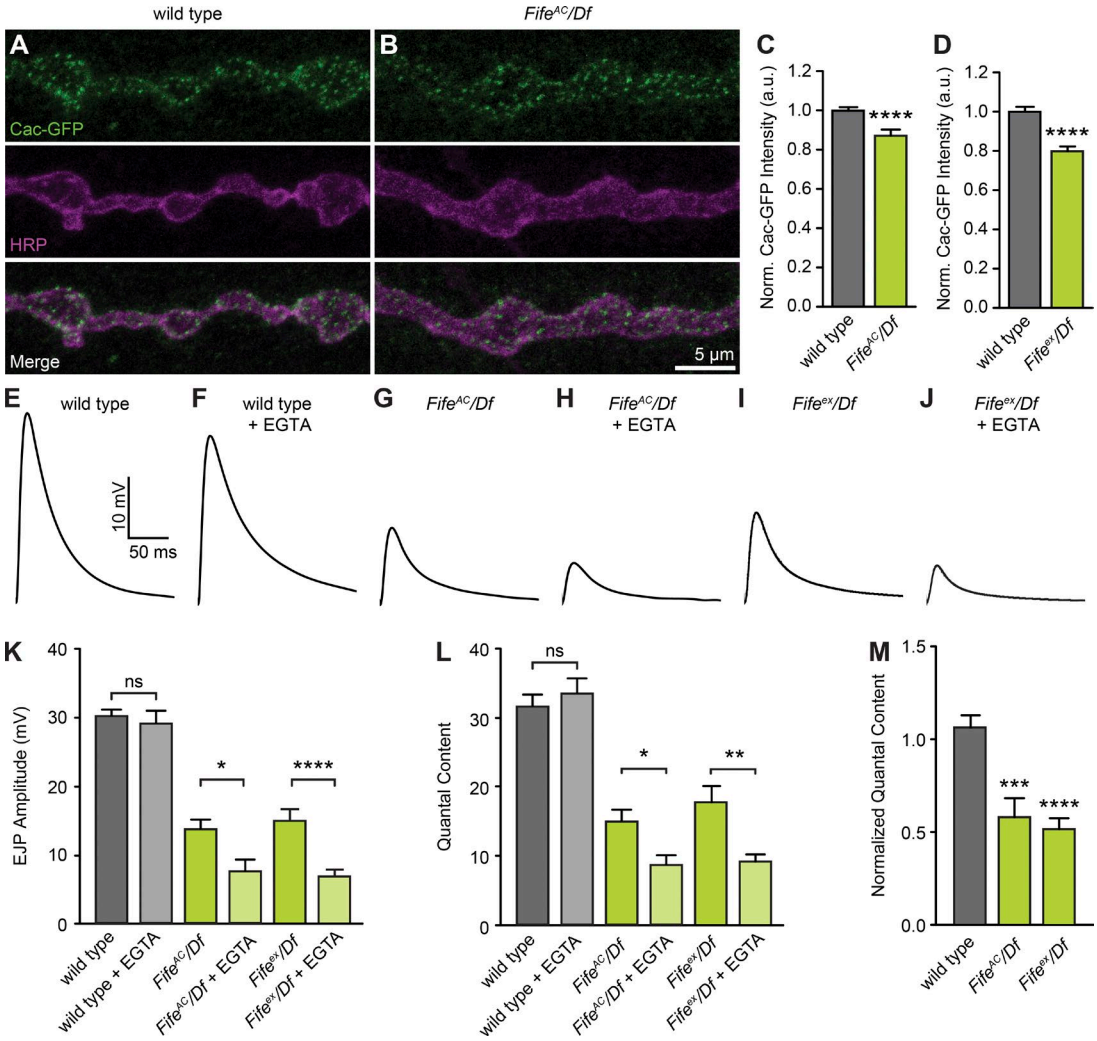

Figure 7. **Fife promotes synaptic vesicle-Ca^{2+} channel coupling.** (A and B) Confocal *z*-projections of Cacophony (Cac)-GFP localization at wild-type (A, *OK6 Gal4*/+; UAS-Cac-GFP/+) and *Fife* (B, *OK6 Gal4*, UAS-Cac-GFP/+; $Fife^{AC}/Df$) NMJs colabeled with antibodies to GFP and HRP. (C and D) Cac-GFP fluorescence intensity normalized to HRP fluorescence intensity is reduced in $Fife^{AC}/Df$ (C, 0.87 ± 0.03 a.u., *n* = 24 NMJs) compared with wild type (1.0 ± 0.02 a.u., *n* = 27 NMJs, P < 0.0001), and similarly in $Fife^{ex}/Df$ (D, 0.80 ± 0.02 a.u., *n* = 20 NMJs) compared with wild type (1.0 ± 0.02 a.u., *n* = 21 NMJs, P < 0.0001). (E–J) Representative traces of EJPs in wild type (E and F), $Fife^{AC}/Df$ (G and H), and $Fife^{ex}/Df$ (I and J) in the absence of EGTA-AM (E, G, and I) and with 10 min pretreatment in 100 µM EGTA-AM (F, H, and J) recorded in HL3 containing 0.6 mM $[Ca^{2+}]_e$. (K and L) Mean EJP amplitude (K) and quantal content (L) are unaffected by exposure to EGTA-AM in wild type (P = 0.60 and 0.47, respectively) but significantly affected in $Fife^{AC}/Df$ (P = 0.010 and 0.015, respectively) and $Fife^{ex}/Df$ (P < 0.0001 and P = 0.004, respectively). (M) Quantal content of EGTA-treated NMJs normalized to untreated controls reveals a significant difference in sensitivity to EGTA between $Fife^{AC}/Df$ and $Fife^{ex}/Df$ and wild type (P = 0.0002 and P < 0.0001, respectively). Wild type: EJP amplitude, 30.16 ± 1.04 mV; quantal content, 31.57 ± 1.68; *n* = 16 NMJs; wild type + EGTA: EJP amplitude, 29.08 ± 1.96 mV; quantal content, 33.53 ± 2.12; *n* = 12 NMJs; $Fife^{AC}/Df$: EJP amplitude, 13.79 ± 1.42 mV; quantal content, 14.99 ± 1.70; *n* = 16 NMJs; $Fife^{AC}/Df$ + EGTA: EJP amplitude, 7.66 ± 1.67 mV; quantal content, 8.66 ± 1.53; *n* = 11 NMJs; $Fife^{ex}/Df$: EJP amplitude, 14.91 ± 1.71 mV; quantal content, 17.82 ± 2.36; *n* = 12 NMJs; and $Fife^{ex}/Df$ + EGTA: EJP amplitude, 6.844 ± 0.99 mV; quantal content, 9.17 ± 1.04; *n* = 16 NMJs. ns, not significant; *, P < 0.05; **, P < 0.01; ***, P < 0.001; ****, P < 0.0001, Student's *t* test or, for non–normally distributed samples, Mann–Whitney *U* test for single comparisons, analysis of variance followed by *post hoc* tests with Šidák correction for multiple comparisons. Error bars represent SEM.

found a similar 20% decrease in Cacophony levels in $Fife^{ex}/Df$ (Fig. 7 D). Thus, there is a small, but consistent, decrease in Ca^{2+} channel levels at *Fife* active zones.

High-probability synchronous release at many synapses, including those of the *Drosophila* NMJ, is thought to be achieved through the nanodomain coupling (generally defined as <100 nm) of molecularly primed synaptic vesicles and clustered Ca^{2+} channels (Kittel et al., 2006; Bucurenciu et al., 2008; Eggermann et al., 2011; Schmidt et al., 2013; Chen et al., 2015; Stanley, 2015). This is consistent with our tomography results showing the majority of docked vesicles residing within 150 nm of the center of the active zone cytomatrix, potentially placing them within ∼100 nm of the Ca^{2+} channels that cluster below the cytomatrix. The loss of these vesicles in *Fife* mutants, together with the trend toward fewer cytomatrix-associated docked vesicles and reduction in active zone clustered Ca^{2+} channels, suggests a key function of Fife may be establishing the nanodomain-coupled vesicle pool.

To functionally assess whether Fife promotes the nanodomain coupling of synaptic vesicles and Ca^{2+} channels, we investigated the effect of EGTA on mutant and wild-type synapses. Because EGTA is a slow Ca^{2+} chelator, it preferentially affects release-ready synaptic vesicles loosely coupled to Ca^{2+} channel clusters (Smith et al., 1984; Eggermann et al.,

Downloaded from http://rupress.org/jcb/article-pdf/216/1/231/1597608/jcb_201601098.pdf by guest on 08 February 2026

2011). Therefore, wild-type synapses exhibiting tight coupling are insensitive to low concentrations of EGTA, whereas neurotransmitter release is diminished at synapses with impaired vesicle-channel coupling. We measured EJP and miniature EJP (mEJP) amplitudes at *Fife* and wild-type NMJs with and without a 10-min pretreatment with 25 µM membrane-permeable EGTA-AM. Consistent with nanodomain coupling at the *Drosophila* NMJ, mean EJP amplitude was unaffected by exposure to EGTA at wild-type NMJs (Fig. 7, E, F, and K). Quantal content was similarly unaffected at wild-type NMJs (Fig. 7, L and M). In contrast, at $Fife^{AC}/Df$ and $Fife^{ex}/Df$ NMJs, EJP amplitude was reduced ∼50% after EGTA exposure (Fig. 7, G–K). Quantal content was similarly reduced, suggesting a severe impairment in the coupling of Ca^{2+} channels and synaptic vesicles (Fig. 7, L and M). Thus, we conclude that Fife regulates neurotransmitter release probability by organizing active zones to promote the docking of synaptic vesicles in close proximity to Ca^{2+} channels clustered at the active zone cytomatrix.

Fife is required for homeostatic plasticity

In addition to establishing baseline neurotransmitter release properties, local molecular determinants of presynaptic properties must be able to modulate synaptic strength in response to functional inputs. One form of presynaptic plasticity, termed homeostasis, functions to maintain neural communication within an established range. At the *Drosophila* NMJ, genetic or pharmacological inhibition of neurotransmitter receptors leads to a rapid increase in neurotransmitter release that precisely offsets the postsynaptic deficit (Frank et al., 2006). To determine whether Fife's role at active zones extends to the modulation of synaptic release properties during homeostasis, we compared the response of wild-type and *Fife* synapses to nonsaturating concentrations of the glutamate receptor antagonist philanthotoxin-433 (PhTx). In wild type and two allelic combinations of *Fife*, the amplitudes of mEJPs were significantly reduced upon PhTx application (Fig. 8, A–G). At wild-type NMJs, EJP amplitude was maintained at normal levels because of a compensatory increase in quantal content (Fig. 8, A, B, H, and I). In contrast, no compensatory increase in neurotransmitter release occurs at *Fife* synapses, so EJP amplitudes are significantly lower than baseline levels (Fig. 8, C–F, H, and I). These data indicate that in addition to its role in establishing synaptic release properties, Fife plays a critical role in modulating synaptic strength to promote synaptic plasticity (Fig. 8 J).

Discussion

Here we demonstrate that Fife plays a key role in organizing presynaptic terminals to determine synaptic release properties. We found that Fife functions with RIM at the active zone cytomatrix to promote neurotransmitter release. Our functional and ultrastructural imaging studies demonstrate that Fife regulates the docking of release-ready synaptic vesicles and, through nanodomain coupling to Ca^{2+} channels, their high probability of release. We further find that Fife is required for the homeostatic increase in neurotransmitter release that maintains circuit function when postsynaptic receptors are disrupted. These findings uncover Fife's role as a local determinant of synaptic strength and add to our understanding of how precise communication in neural circuits is established and modulated (Fig. 8 J).

Our finding that Fife interacts with RIM provides insight into how Fife functions within the network of cytomatrix proteins (Figs. 1 and 2). RIM is a central active zone protein that was recently shown to facilitate vesicle priming at mammalian synapses by relieving autoinhibition of the priming factor Munc13 (Deng et al., 2011). Like Fife, *Drosophila* RIM promotes Ca^{2+} channel accumulation at active zones and exhibits EGTA-sensitive neurotransmitter release at the *Drosophila* NMJ (Graf et al., 2012; Müller et al., 2012). This suggests that Fife and RIM may promote high-probability neurotransmitter release by acting together to dock and prime synaptic vesicles in close proximity to Ca^{2+} channels clustered at the cytomatrix. Our findings are consistent with previous work in pancreatic β cells, where it was found that Piccolo and RIM2α form a complex that promotes insulin secretion through an unknown mechanism (Coppola et al., 2001; Fujimoto et al., 2002). To date, functional studies at mammalian synapses have focused on investigating interactions between Piccolo and Bassoon, which bind through their common coiled-coil regions. Thus, it will be of interest to investigate the functional relationship between Piccolo and RIM in promoting neurotransmitter release in mouse models. Piccolo also binds CAST1 through coiled-coil domain interactions (Wang et al., 2009). Although the Piccolo coiled-coil region is not present in Fife, future studies to determine whether this interaction is preserved through distinct interacting domains will be important, as Fife and *Drosophila* CAST-related Bruchpilot carry out overlapping functions (Kittel et al., 2006; Matkovic et al., 2013). Similarly, although neither Fife nor Piccolo contains the conserved SH3-binding domain that mediates the interaction between RIM and RIM-binding protein, the overlap between *Fife* and *RIM-binding protein* phenotypes raises the possibility of functional interactions that will also be important to investigate in future experiments (Liu et al., 2011; Müller et al., 2015).

We observed significant alterations to active zone cytomatrix size and structure in *Fife* mutants, whereas none have been detected in *RIM* mutants, indicating that Fife carries out this function independently of RIM (Fig. 3; Graf et al., 2012; Müller et al., 2012). Our previous ultrastructural analysis in aldehyde-fixed samples revealed occasional free-floating electron-dense structures that resemble active zone cytomatrix material and cluster synaptic vesicles (Bruckner et al., 2012). These unanchored electron-dense structures have also been observed at low frequency in *Drosophila RIM-binding protein* mutants, which, like *Fife* mutants, exhibit smaller active zone cytomatrices, and at higher frequency in rodent ribbon synapses lacking Bassoon (Dick et al., 2003; Khimich et al., 2005; Frank et al., 2010; Liu et al., 2011). These structures were not visible in our HPF/FS-prepared electron microscopy samples, likely because protein components of the synapse are not cross-linked upon fixation. That these structures are not observed in control synapses but have been found in multiple active zone cytomatrix mutants argues that the extensive cross-linking of proteins in chemically fixed preparations may enable the visualization of biologically relevant complexes missed with cryofixation. This supports the idea that the two fixation methods may offer different advantages for ultrastructural studies of synapses (Südhof, 2012). In any case, the active zone cytomatrix is significantly reduced in size at *Fife* active zones in both HPF/FS- and aldehyde-fixed electron micrographs (Fig. 3).

Although diminished or absent cytomatrices have been observed in electron micrographs of RIM-binding protein and

Downloaded from http://rupress.org/jcb/article-pdf/216/1/231/1597608/jcb_201601098.pdf by guest on 08 February 2026

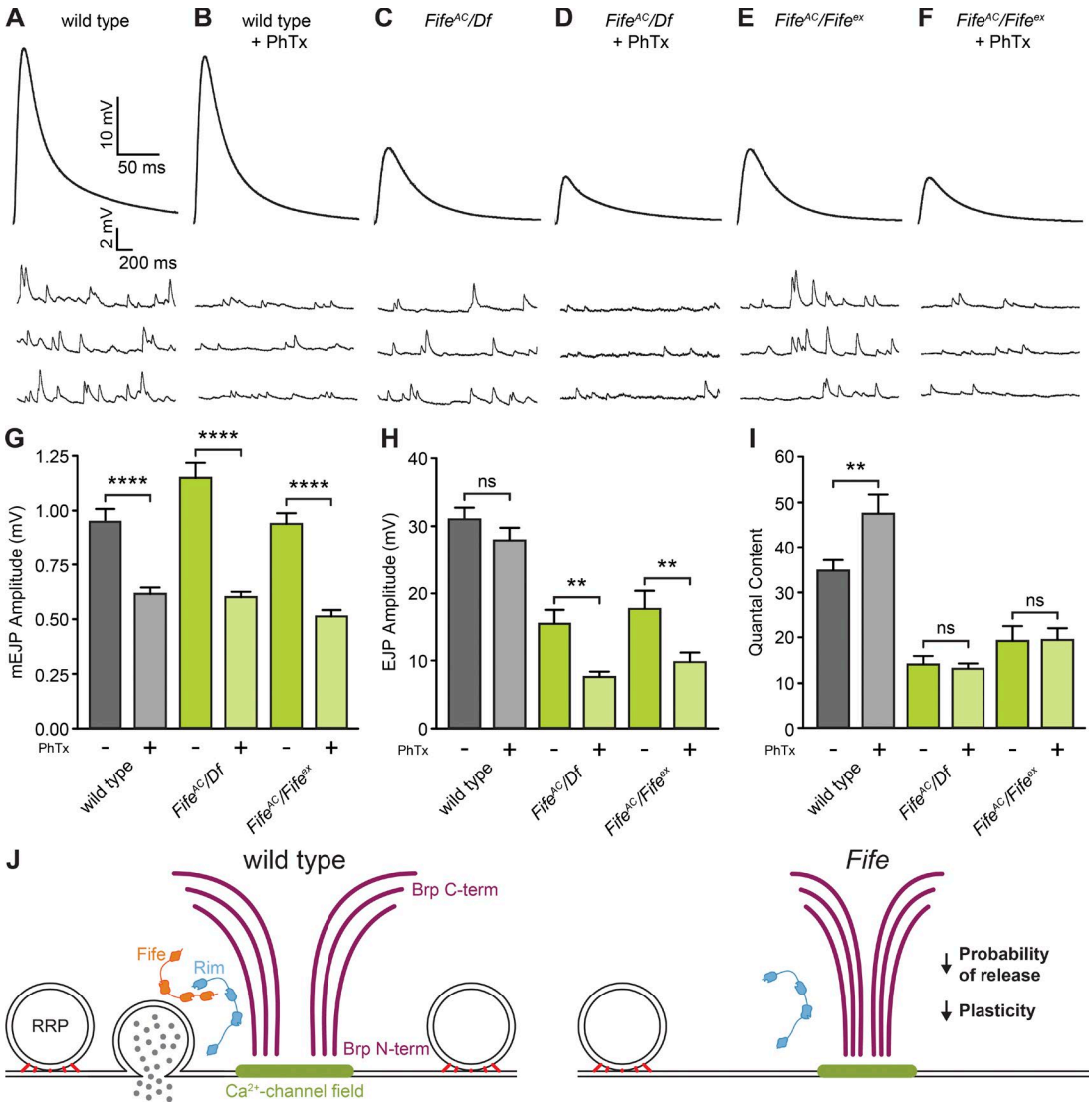

Figure 8. **Fife regulates homeostatic plasticity.** (A–F) Representative traces of EJPs and mEJPs recorded in 0.6 mM Ca^{2+} with (B, D, and F) or without (A, C, and E) pretreatment in HL3 containing 20 µM PhTx at wild-type (A and B), *Fife*^{AC}/*Df* (C and D), and *Fife*^{AC}/*Fife*^{ex} (E and F) NMJs. Stimulus artifacts have been removed for clarity. (G) Pretreatment in HL3 containing 20 µM PhTx significantly reduces mEJP amplitude in wild type, *Fife*^{AC}/*Df*, and *Fife*^{AC}/*Fife*^{ex} (wild type, 0.95 ± 0.06 mV, *n* = 22 NMJs; wild type + PhTx, 0.61 ± 0.03 mV, *n* = 14 NMJs, P < 0.0001; *Fife*^{AC}/*Df*, 1.15 ± 0.07 mV, *n* = 12 NMJs; *Fife*^{AC}/*Df* + PhTx, 0.60 ± 0.02 mV, *n* = 14 NMJs, P < 0.0001; *Fife*^{AC}/*Fife*^{ex}, 0.94 ± 0.08 mV, *n* = 11 NMJs; *Fife*^{AC}/*Fife*^{ex} + PhTx, 0.51 ± 0.03 mV, *n* = 12 NMJs, P < 0.0001). (H) Pretreatment in HL3 containing 20 µM PhTx significantly reduces EJP amplitude in *Fife*^{AC}/*Df* and *Fife*^{AC}/*Fife*^{ex}, but not wild type (wild type, 30.98 ± 1.71 mV, *n* = 22 NMJs; wild type + PhTx, 27.83 ± 0.1.83 mV, *n* = 14 NMJs, P = 0.23; *Fife*^{AC}/*Df*, 15.50 ± 1.97 mV, *n* = 12 NMJs; *Fife*^{AC}/*Df* + PhTx, 7.61 ± 0.76 mV, *n* = 14 NMJs, P = 0.0017; *Fife*^{AC}/*Fife*^{ex}, 17.65 ± 1.54 mV, *n* = 11 NMJs; *Fife*^{AC}/*Fife*^{ex} + PhTx, 9.83 ± 1.37 mV, *n* = 12 NMJs, P = 0.0010). (I) Pretreatment in HL3 containing 20 µM PhTx significantly increases quantal content in wild type but not in *Fife*^{AC}/*Df* or *Fife*^{AC}/*Fife*^{ex} (wild type, 34.74 ± 2.45, *n* = 22 NMJs; wild type + PhTx, 47.33 ± 4.25, *n* = 14 NMJs, P = 0.0092; *Fife*^{AC}/*Df*, 13.99 ± 1.88, *n* = 12 NMJs; *Fife*^{AC}/*Df* + PhTx, 12.98 ± 1.37, *n* = 14 NMJs, P = 0.53; *Fife*^{AC}/*Fife*^{ex}, 19.28 ± 1.66, *n* = 11 NMJs; *Fife*^{AC}/*Fife*^{ex} + PhTx, 19.39 ± 2.67, *n* = 12 NMJs, P = 0.83). Statistical significance represents comparison to untreated in the same genotype. ns, not significant; **, P < 0.01; ****, P < 0.0001; Student's *t* test with Welch's correction if unequal variance; Mann–Whitney test for non–normally distributed datasets. Error bars represent SEM. (J) Model of Fife function. At wild-type active zones, vesicles of the readily releasable pool (RRP) are docked at the presynaptic membrane and molecularly primed (red) within nanometer distance of clustered Ca^{2+} channels (green) clustered beneath the active zone cytomatrix. Loss of Fife function impairs the size and molecular organization of the active zone cytomatrix and, through modulation of the number of readily releasable synaptic vesicles and their coupling to clustered Ca^{2+} channels, the probability of neurotransmitter release and its homeostatic modulation.

Bruchpilot mutants, this phenotype has not been observed in electron micrographs of other active zone cytomatrix mutants, suggesting it represents more than the loss of a single component protein (Kittel et al., 2006; Liu et al., 2011; Graf et al., 2012; Müller et al., 2012; Böhme et al., 2016). Rather, the reduced complexity visible in electron micrographs likely reflects a broader underlying molecular disorganization. Further support for this model comes from superresolution imaging, which reveals molecular disorganization at *Fife* active zones as indicated by the loss of the characteristic ring-shaped localization pattern of Bruchpilot's C terminus (Fig. 3; Kittel et al., 2006). Similar disorganization of Bruchpilot was observed at active zones lacking RIM-binding protein (Liu et al., 2011). We also used superresolution imaging to investigate the localization of active zone proteins Cacophony and RIM-binding protein and, although the levels of Cacophony are reduced at

Downloaded from http://rupress.org/jcb/article-pdf/216/1/231/1597608/jcb_201601098.pdf by guest on 08 February 2026

Fife active zones, we observed no apparent differences in the patterns of these proteins (Fig. 7 and not depicted). Cacophony and RIM-binding protein both localize in smaller puncta than Bruchpilot, so future studies with higher resolution imaging modalities such as stimulated emission depletion microscopy may reveal more subtle abnormalities. Correlations between active zone molecular composition and release probability have been observed at diverse synapses (Harris and Stevens, 1989; Murthy et al., 2001; Matz et al., 2010; Peled and Isacoff, 2011; Weyhersmüller et al., 2011; Holderith et al., 2012; Matkovic et al., 2013; Ehmann et al., 2014). At the *Drosophila* NMJ, functional imaging with genetically encoded Ca^{2+} indicators has demonstrated that active zones display a wide range of release probabilities (Guerrero et al., 2005; Melom et al., 2013). Active zones with high release probability contain higher levels of Bruchpilot, which may in turn correlate with higher Ca^{2+} channel levels (Fouquet et al., 2009; Graf et al., 2009; Peled and Isacoff, 2011). At mouse hippocampal synapses, Bassoon and RIM levels directly correlate with neurotransmitter release probability (Matz et al., 2010; Holderith et al., 2012). Consistently, synaptic probability of release is significantly decreased in *Fife* mutants (Fig. 4).

Through a combination of morphological and functional studies, we found that Fife acts to promote the active zone docking of synaptic vesicles and regulates their probability of release (Figs. 5, 6, and 7). Because the number of readily releasable vesicles appears to scale with active zone cytomatrix size and molecular composition at diverse synapses, a conserved function of the active zone cytomatrix may be to establish release sites for synaptic vesicles (Cao et al., 2004; Fouquet et al., 2009; Branco et al., 2010; Frank et al., 2010; Hallermann et al., 2010a; Weyhersmüller et al., 2011; Holderith et al., 2012; Matkovic et al., 2013; Ehmann et al., 2014). Consistent with this view, the number of release-ready vesicles is also reduced in *Drosophila RIM-binding protein*–null mutants and isoform-specific *bruchpilot*$^{\Delta 170}$ and *bruchpilot*$^{\Delta 190}$ mutants, which share similar active zone structural abnormalities with *Fife* (Liu et al., 2011; Matkovic et al., 2013). By combining rapid preservation of intact *Drosophila* larvae by HPF/FS fixation, electron tomography, and extensive segmentation of active zone structures, we obtained a detailed view of the 3D organization of active zones in near-native state that allowed us to further dissect Fife's role in determining the size of the readily releasable vesicle pool (Fig. 6). Membrane-docked vesicles are significantly decreased in *Fife* mutants, whereas more distant vesicles attached to the membrane by long tethers appear unaffected (Fig. 6). Correlating physiological and morphological parameters of neurotransmission is an ongoing challenge in the field. It has been proposed that docking and priming are not separable events in the establishment of the readily releasable vesicle pool, but rather the morphological and physiological manifestations of a single process (Siksou et al., 2009; Imig et al., 2014). Although approximately one third of docked vesicles in our preparations lack obvious short connections to the membrane, which are thought to represent priming factors, we cannot exclude the possibility that these filaments are present but obscured, perhaps because the vesicles are more tightly linked to the membrane (Siksou et al., 2009; Fernández-Busnadiego et al., 2010). As this proportion is unchanged in *Fife* mutants, we conclude that Fife acts to promote vesicle docking and may simultaneously facilitate molecular priming—possibly through its interactions with RIM.

Our data indicate that neurotransmitter release at Fife synapses is highly sensitive to EGTA, a slow Ca^{2+} chelator that has been used to investigate the coupling of Ca^{2+} influx at voltage-gated Ca^{2+} channels and Ca^{2+} sensors on synaptic vesicles (Fig. 7; Smith et al., 1984; Eggermann et al., 2011). At synapses with high release probability, including inhibitory synapses in the mammalian hippocampus and cerebellum, excitatory synapses of the mature Calyx of held, and the *Drosophila* NMJ, molecularly primed synaptic vesicles and Ca^{2+} channel clusters are thought to be positioned within ∼100 nm of one another to ensure the tight coupling of Ca^{2+} influx and Ca^{2+} sensors that explains observed release properties (Eggermann et al., 2011). The EGTA sensitivity of release at *Fife*, but not wild-type, NMJs indicates that Fife likely regulates the probability that a docked vesicle is released by positionally coupling release-ready vesicles to Ca^{2+} channels clustered beneath the active zone cytomatrix (Fig. 7). The trend toward fewer docked vesicles associated with the active zone cytomatrix in tomograms of *Fife* synapses provides morphological support for this model (Figs. 6 and 7). Building on detailed tomographic studies of the *Drosophila* NMJ to visualize how Ca^{2+} channels and vesicles are spatially organized at active zones in different genetic backgrounds will be an important step in advancing our understanding of the geometry of release probability and how it is established.

Finally, we find that Fife is required for presynaptic homeostasis (Fig. 8). In response to decreases in glutamate receptor levels or function, *Drosophila* motoneurons rapidly increase synaptic vesicle release to maintain postsynaptic excitation (Petersen et al., 1997; Frank et al., 2006). This homeostatic increase in presynaptic neurotransmission is accompanied by an increase in the number of dense projections per active zone and Bruchpilot levels (Reiff et al., 2002; Weyhersmüller et al., 2011). Cytomatrix proteins RIM, RIM-binding protein, and now Fife have all been shown to function in presynaptic homeostasis, indicating a critical role for the active zone cytomatrix as a substrate for synaptic plasticity (Fig. 8; Müller et al., 2012, 2015). Our studies provide insight into the molecular mechanisms through which the active zone cytomatrix determines neurotransmitter release parameters to modulate how information flows in neural circuits.

Materials and methods

Drosophila genetics and genome engineering

The following fly lines are available at the Bloomington Drosophila Stock Center (BDSC): *w*^{1118} (BDSC #5905)*; Fife deficiencies* Df(3L) Exel6091 (BDSC #7570) and Df(3L)BSC412 (BDSC #24916); neuronal Gal4 drivers *C155-Gal4* (BDSC #458) and *OK6-Gal4* (BDSC #64199); and *vasa-Cas9* (BDSC #51324). *Fife*^{ex1027}, described in Bruckner et al. (2012) and referred to here as *Fife*^{ex}, is a 16.5-kb deletion generated by Minos element excision that behaves as a genetic null. UAS-FLAG-Fife flies were generated by cloning full-length *Fife* coding sequence into the pTFW vector (Drosophila Gateway Vector Collection, Carnegie Institution for Science). UAS-RIM-GFP flies were provided by the DiAntonio laboratory (Graf et al., 2012). *RIM*^{ex73} and *RIM*^{ex103} were provided by the DiAntonio and Davis laboratories, respectively (Graf et al., 2012; Müller et al., 2012). An independent *Fife*-null allele, *Fife*^{AC}, was generated via CRISPR-mediated homology-directed repair (Gratz et al., 2014). Two targeting guide RNAs and a donor plasmid containing 1-kb homology arms flanking an attP, 3xP3-DsRed cassette were injected into *vasa-Cas9* embryos.

Downloaded from http://rupress.org/jcb/article-pdf/216/1/231/1597608/jcb_201601098.pdf by guest on 08 February 2026

This resulted in a 25.6-kb deletion of the Fife locus extending from bp 2,664,461 to 2,690,083 that removes the first 12 coding exons of *Fife*. Engineered lines were identified by DsRed expression in the eye and confirmed molecularly. The null phenotype was confirmed through electrophysiological analysis of neurotransmitter release (Fig. 1, G and H). We used a similar approach to insert tags at multiple sites in the *Fife* locus (http://www.flyCRISPR.molbio.wisc.edu). In brief, sequences coding for a GFP or HA peptide tag flanked by flexible linkers were inserted at the N terminus or into exon 6 of the endogenous *Fife* locus, respectively, along with a selectable marker flanked by piggyBac inverted terminal repeat sequences. piggyBac transposase was subsequently used for footprint-free removal of the marker, followed by molecular confirmation of precise tag incorporation.

Electrophysiology

Male third-instar larvae were dissected in Ca^{2+}-free hemolymph-like saline (HL3; 70 mM NaCl, 5 mM KCl, 20 mM $MgCl_2$, 10 mM $NaHCO_3$, 115 mM sucrose, 5 mM trehalose, and 5 mM Hepes, pH 7.2; Stewart et al., 1994). Recordings were performed in HL3 containing 0.6 mM Ca^{2+} unless otherwise indicated. A sharp borosilicate electrode (resistance of 15–25 MΩ) filled with 3 M KCl was used to record from muscle 6 of segments A3 and A4. All dissections and recordings were performed at 25°C, and all cells analyzed had an initial resting potential between −60 and −80 mV and input resistance ≥5 MΩ. For each cell, 60 consecutive mEJPs were collected with pClamp and analyzed using MiniAnalysis to obtain mean amplitude and frequency. EJPs were stimulated by applying a 1-ms pulse to the cut end of the segmental nerve innervating the impaled muscle cell. Stimulus amplitude was adjusted to reliably recruit both the 1s and 1b inputs onto muscle 6. 100 consecutive EJPs were recorded for each cell and analyzed in pClamp to obtain mean EJP amplitude. Quantal content was calculated for each NMJ as mean EJP amplitude divided by mean mEJP amplitude.

For paired-pulse recordings, stimulus amplitude was adjusted to recruit 1s and 1b nerve inputs, and five stimuli were applied at 20 Hz. Each NMJ was stimulated with ten 20-Hz trains, with 5 s of rest between each train. Trains were averaged for each cell, and the mean amplitude of each EJP was measured.

The size of the release-ready vesicle pool was estimated using linear back extrapolation of cumulative quantal content during high-frequency stimulus trains in two-electrode voltage clamp recordings conducted in HL3 containing 1 mM Ca^{2+}. In brief, muscle 6 of abdominal segments A3 and A4 was impaled with voltage monitoring (resistance 15–25 MΩ) and current passing (resistance 7–12 MΩ) sharp electrodes filled with 3 M KCl. Measurements of initial resting potential did not differ by more than 5 mV between the two electrodes, and cells with an initial resting potential more than −50 mV or input resistance ≤5 MΩ were rejected. Cells were clamped at −70 mV for both EJC and mEJC recordings, and clamp gain was adjusted to achieve voltage error of 1–5%. Holding current did not exceed −5 nA. EJCs were evoked by applying 1-ms pulses to the cut end of the appropriate segmental nerve, and stimulus amplitude was adjusted to reliably recruit the combined 1s and 1b inputs. 1-ms pulses were applied at 60 Hz, and the amplitude of each EJC from peak to baseline immediately before each stimulus was measured in Clampfit. Two *Fife* cells that did not depress were excluded from the analysis to prevent underestimation of pool size. Quantal content during the high-frequency train was calculated by dividing the amplitude of each EJC in the train by the mean mEJC amplitude from that cell. The apparent size of the release-ready pool was estimated for each NMJ by a linear fit to the last 10 of 30 quantal content measurements in each 60-Hz train, when a steady-state of neurotransmitter release from the recycling pool had been reached, and back extrapolating to time zero.

The effect of slow Ca^{2+}-chelation on neurotransmitter release was assessed by pretreating dissected preparations with cell-permeable EGTA-AM (Thermo Fisher Scientific). EGTA-AM was diluted to 25 mM in DMSO, aliquoted, and stored at −20°C. Stock solutions were thawed immediately before use, diluted to 25 µM in Ca^{2+}-free HL3, and applied to the filleted larval body wall for 10 min. After treatment, preparations were washed for 5 min in HL3 with Ca^{2+} before recording EJP and mEJP amplitudes as described for recordings of baseline neurotransmission.

Pharmacological homeostatic challenge was assessed by incubating semi-intact preparations in 20 µM PhTx diluted in HL3 for 10 min at 25°C (Frank et al., 2006). After pretreatment, the dissection was completed and the preparation was rinsed five times in recording solution. During the dissection, extreme care was taken to avoid excessive stretching of body wall muscles, as this may significantly impair induction of homeostasis (Frank et al., 2006).

Immunohistochemistry

Male third-instar larvae were dissected in ice-cold Ca^{2+}-free saline and fixed for 10 min in 4% PFA in PBS. Dissected larvae were washed and permeabilized in PBS containing 0.1% Triton X-100 and blocked overnight at 4°C in PBS containing 0.1% Triton X-100 and 1% BSA. Dissected larvae were incubated in primary antibodies overnight at 4°C or 3 h at RT and secondary antibodies for 2 h at RT, and then mounted in Vectashield (Vector Laboratories) or ProLong Diamond (Thermo Fisher Scientific). The following antibodies were used in this study at the indicated concentrations: mouse anti-Bruchpilot at 1:100 (Nc82; developed by Erich Buchner and obtained from the Developmental Studies Hybridoma Bank), mouse anti-FLAG at 1:500 (M2; Sigma-Aldrich), rabbit anti-GFP conjugated to Alexa Fluor 488 at 1:500 (#A21311; Thermo Fisher Scientific), rabbit anti-HA at 1:500 (C29F4; Cell Signaling Technology), and anti-HRP conjugated to Alexa Fluor 647 at 1:500 (Jackson ImmunoResearch Laboratories, Inc.). Species-specific Alexa Fluor 488 and 568 secondary antibodies (Invitrogen) were used at 1:500.

Confocal imaging and analysis

Confocal images were acquired on an LSM 510 (ZEISS) with Plan-Apo 63× (1.40 NA) oil-immersion objective, A1R-Si+ (Nikon) with Plan-Apo 60× (1.40 NA) oil-immersion objective, or Fluoview FV1000 (Olympus) with Plan-Apo 60× (1.42 NA) oil-immersion objective. Brightness and contrast were adjusted using the Fiji distribution of ImageJ (Schindelin et al., 2012). For analysis of Cacophony puncta intensity, all genotypes were stained together and imaged with identical settings. For consistency, analysis was limited to NMJ 4 in segments A2 and A3. To measure Cac-GFP and HRP intensity, nonsynaptic structures including axons were removed from the images using free-hand selection and fill. *z*-stacks were flattened using the Maximum Intensity Z-projection function. Channels were separated and a threshold was applied to remove irrelevant lower-intensity pixels. Separation of individual puncta was facilitated by the Find Maxima tool in Fiji. Intensity data were collected using the Analyze Particles tool.

SIM imaging and analysis

SIM images were acquired on an N-SIM microscope (Nikon) equipped with a 100× (1.49 NA) Apo TIRF oil-immersion objective (Nikon) and an iXon 897 EMCCD camera (Andor Technology). Images were reconstructed and analyzed using NIS-Elements Ar (Nikon) and Fiji software. For analysis of Bruchpilot morphology, *z*-stacks were flattened using the Maximum Intensity Z-projection function and background subtracted using the rolling ball method in Fiji. For each NMJ image, ∼20 central Bruchpilot punctae in planar orientation were selected,

Downloaded from http://rupress.org/jcb/article-pdf/216/1/231/1597608/jcb_201601098.pdf by guest on 08 February 2026

blind to genotype, for analysis. For each active zone, a fluorescence intensity profile plot was generated in Fiji along a 1-µm line drawn along the longest axis through the center of the Bruchpilot spot.

HPF/FS

HPF and FS were optimized based on previous work in both *C. elegans* and *Drosophila* (Rostaing et al., 2004; Fouquet et al., 2009; Gracheva et al., 2010; Stigloher et al., 2011; McDonald et al., 2012). Late second-instar larvae were placed in the 200-µm cavity of aluminum specimen carriers (Type A, with the flat side of Type B carriers used as a lid; Technotrade International) filled with a mixture of 10% BSA (Sigma-Aldrich) and OP50 *E. coli* in PBS. Specimen carriers were pretreated with 1-Hexadecene (Sigma-Aldrich) to adequately seal the freezing chamber. HPF was performed with a Bal-Tec HPM-010 apparatus at a freezing speed >20,000 K/s and pressure >2,000 bar. FS was performed in a Leica EM AFS1, where samples were incubated in 0.5% glutaraldehyde, 0.1% tannic acid, and 1% H_2O in anhydrous acetone for 98 h at −90°C, rinsed with 1% H_2O in acetone for 2 h at −90°C followed by incubation in 1% OsO4 and 1% H_2O in acetone for 7 h at −90°C. Samples were warmed to −20°C over 14 h (5°C/h), then incubated at −20°C for 16 h. Temperature was increased to 4°C over 2.4 h (10°/h). Finally, samples were rinsed with 1% H_2O in acetone for 2 h, transferred to RT, and embedded in epon using standard procedures.

Electron microscopy

Ultrathin sections (gray-silver) were collected on Pioloform-coated copper slot grids and stained with 8% uranyl acetate in 50% ethanol and Reynold's lead citrate. Images were collected on a Phillips CM120 transmission electron microscope at 80 KeV. T-bar width and the number of synaptic vesicles within 5 nm of the active zone membrane were quantified in random ultrathin sections blind to genotype.

Electron tomography

For electron tomography, 250-nm sections were cut, collected onto Pioloform-coated copper slot grids, and stained with 2% aqueous uranyl acetate and Reynold's lead. For fiducial-aided image alignment, grids were treated with 10-nm Aurion Gold solution (Electron Microscopy Sciences). Freezing quality was evaluated by surveying the preservation of muscle cell nuclei, which are sensitive to ice crystal formation, and damaged specimens were excluded. Boutons were preselected using a Phillips CM120 transmission electron microscope at 80 KeV. Serial tilt acquisition was automatically conducted at 300 KeV from −60° to 60° in 1° increments at a nominal magnification of 31,000× using SerialEM software (Mastronarde, 2005) on an FEI TF-30 transmission electron microscope equipped with a Gatan 2k × 2k ultrascan camera. Tilt-image series were aligned using fiducial-guided alignment, and virtual slices were computationally generated using ETomo/IMOD (Kremer et al., 1996). For double-tilt tomograms, samples were rotated 90°, and an additional serial tilt series was acquired with identical acquisition settings in 1° increments from −40° to 40°, −50° to 50°, or −60° to 60°, depending on the position of the sample within each grid.

Segmentation and quantification of tomograms

Segmentation and quantification of electron tomograms was conducted using Amira 6.0.1 (FEI Software). 29 tomograms (16 wild type and 13 *Fife*) were fully segmented for membrane-connected synaptic vesicles. Synaptic vesicles were annotated with the spherical landmark tool, and each landmark was adjusted according to the maximum visible vesicle diameter. Quantification and distribution of synaptic vesicles in direct contact with the active zone membrane (docked vesicles) were quantified, blind to genotype, in 23 double-tilt tomograms (14 wild type and 9 *Fife*) because the high resolution allowed us to unambiguously distinguish membrane-associated from membrane-proximal vesicles. To measure the distance of docked vesicles to the center of the active zone cytomatrix, a point was placed at center of the dense projection core, and the shortest distance in three dimensions between the membrane of each docked synaptic vesicle and this point was measured. Three tomograms of each genotype were further segmented to fully reveal the active zone cytomatrix. Dense projections were defined using an Amira "labelfield," where they were segmented using a region growing tool and magic wand to adjust gray value threshold and unambiguously detect the full extent of the dense projection in each virtual slice based on pixel density. The same method was also applied to segment the filaments of varying length linking synaptic vesicles to the presynaptic membrane.

Coimmunoprecipitation

S2 cells were transfected with Fife C2A, Fife C2B, or RIM C2B tagged with FLAG or HA as indicated. Transfected cells were lysed in S2 lysis buffer (100 mM KCl, 20 mM Hepes, pH 7.5, 5% glycerol, 0.5% Triton X-100, and protease inhibitor cocktail). For FLAG immunoprecipitation, lysates were incubated with 4 µg of either IgG or FLAG M2 (Sigma-Aldrich) antibody overnight at 4°C, followed by incubation at 4°C for 2 h with Protein A/G agarose beads (Thermo Fisher Scientific). For HA immunoprecipitation, lysates were incubated with 40 µl of anti-HA affinity matrix (3F10; Roche) for 2–3 h at 4°C. Beads were washed and resuspended in 1× SDS-PAGE loading buffer for Western blot analysis. Each interaction was repeated in three experiments.

Statistical analyses

Single comparisons of normally distributed datasets were conducted by Student's *t* test. Welch's correction was used in cases of unequal variance. The Mann-Whitney *U* test was used for single comparisons of non-normally distributed data. Multiple comparisons were performed by analysis of variance followed by post hoc tests with Šidák correction.

Online supplemental material

Figure S1 shows that the RIM C2B domain coimmunoprecipitates the C2A and C2B domains of Fife. Video 1 shows a virtual slice stack through an electron tomogram of a wild-type active zone. Video 2 shows the segmentation of active zone features from tomogram virtual slices of a wild-type active zone. Video 3 shows a virtual slice stack through an electron tomogram of a *Fife* active zone.

Acknowledgments

We thank Graeme Davis, Aaron DiAntonio, the Developmental Studies Hybridoma Bank, the Bloomington Drosophila Stock Center, and the Drosophila Genomics Resource Center for antibodies, fly stocks, and plasmids. We thank Elle Grevstad and the University of Wisconsin-Madison Biochemistry Optical Core for assistance with SIM and Ben August, Alex Kvit, the University of Wisconsin Medical School Electron Microscope Facility, and the University of Wisconsin-Madison Materials Science Center for excellent technical assistance with electron microscopy. Janet Richmond, Szi-Chieh Yu, and Shigeki Watanabe provided invaluable advice on HPF/FS techniques. We are grateful to Desiree Benefield and Janice Pennington for their expert guidance on electron tomography and to Marisa Otegui, Paul Ahlquist, Bill Hickey, and Sean Carroll for generously sharing equipment. We thank Heather Broihier, Richard Daniels, and members of the O'Connor-Giles laboratory for critical comments on the manuscript and insightful discussions.

This work was supported by grants from the National Institutes of Health (R01NS078179 and R21NS088830) and the McKnight

Downloaded from http://rupress.org/jcb/article-pdf/216/1/231/1597608/jcb_201601098.pdf by guest on 08 February 2026

Foundation to K.M. O'Connor-Giles and a National Science Foundation Graduate Research Fellowship to J.J. Bruckner. Trainee support to S.J. Gratz was provided by the University of Wisconsin-Madison Predoctoral Training Program in Genetics (T32GM007133).

The authors declare no competing financial interests.

Author contributions: J.J. Bruckner, S.J. Gratz, and K.M. O'Connor-Giles conceived of the study; J.J. Bruckner, H. Zhan, S.J. Gratz, M. Rao, F. Ukken, and G. Zilberg performed experiments; J.J. Bruckner, H. Zhan, S.J. Gratz, and K.M. O'Connor-Giles analyzed data; and J.J. Bruckner, H. Zhan, S.J. Gratz, and K.M. O'Connor-Giles wrote the manuscript.

Submitted: 27 January 2016
Revised: 19 October 2016
Accepted: 29 November 2016

References

Ackermann, F., C.L. Waites, and C.C. Garner. 2015. Presynaptic active zones in invertebrates and vertebrates. *EMBO Rep.* 16:923–938. http://dx.doi.org/10.15252/embr.201540434

Alabi, A.A., and R.W. Tsien. 2012. Synaptic vesicle pools and dynamics. *Cold Spring Harb. Perspect. Biol.* 4:a013680. http://dx.doi.org/10.1101/cshperspect.a013680

Aravamudan, B., T. Fergestad, W.S. Davis, C.K. Rodesch, and K. Broadie. 1999. *Drosophila* UNC-13 is essential for synaptic transmission. *Nat. Neurosci.* 2:965–971. http://dx.doi.org/10.1038/14764

Ariel, P., M.B. Hoppa, and T.A. Ryan. 2013. Intrinsic variability in Pv, RRP size, Ca^{2+} channel repertoire, and presynaptic potentiation in individual synaptic boutons. *Front. Synaptic Neurosci.* 4:9. http://dx.doi.org/10.3389/fnsyn.2012.00009

Böhme, M.A., C. Beis, S. Reddy-Alla, E. Reynolds, M.M. Mampell, A.T. Grasskamp, J. Lützkendorf, D.D. Bergeron, J.H. Driller, H. Babikir, et al. 2016. Active zone scaffolds differentially accumulate Unc13 isoforms to tune Ca^{2+} channel-vesicle coupling. *Nat. Neurosci.* 19:1311–1320. http://dx.doi.org/10.1038/nn.4364

Branco, T., V. Marra, and K. Staras. 2010. Examining size-strength relationships at hippocampal synapses using an ultrastructural measurement of synaptic release probability. *J. Struct. Biol.* 172:203–210. http://dx.doi.org/10.1016/j.jsb.2009.10.014

Brandt, A., D. Khimich, and T. Moser. 2005. Few $Ca_V1.3$ channels regulate the exocytosis of a synaptic vesicle at the hair cell ribbon synapse. *J. Neurosci.* 25:11577–11585. http://dx.doi.org/10.1523/JNEUROSCI.3411-05.2005

Bruckner, J.J., S.J. Gratz, J.K. Slind, R.R. Geske, A.M. Cummings, S.E. Galindo, L.K. Donohue, and K.M. O'Connor-Giles. 2012. Fife, a *Drosophila* Piccolo-RIM homolog, promotes active zone organization and neurotransmitter release. *J. Neurosci.* 32:17048–17058. http://dx.doi.org/10.1523/JNEUROSCI.3267-12.2012

Bruckner, J.J., H. Zhan, and K.M. O'Connor-Giles. 2015. Advances in imaging ultrastructure yield new insights into presynaptic biology. *Front. Cell. Neurosci.* 9:196. http://dx.doi.org/10.3389/fncel.2015.00196

Bucurenciu, I., A. Kulik, B. Schwaller, M. Frotscher, and P. Jonas. 2008. Nanodomain coupling between Ca^{2+} channels and Ca^{2+} sensors promotes fast and efficient transmitter release at a cortical GABAergic synapse. *Neuron.* 57:536–545. http://dx.doi.org/10.1016/j.neuron.2007.12.026

Bucurenciu, I., J. Bischofberger, and P. Jonas. 2010. A small number of open Ca^{2+} channels trigger transmitter release at a central GABAergic synapse. *Nat. Neurosci.* 13:19–21. http://dx.doi.org/10.1038/nn.2461

Cao, Y.-Q., E.S. Piedras-Rentería, G.B. Smith, G. Chen, N.C. Harata, and R.W. Tsien. 2004. Presynaptic Ca^{2+} channels compete for channel type-preferring slots in altered neurotransmission arising from Ca^{2+} channelopathy. *Neuron.* 43:387–400. http://dx.doi.org/10.1016/j.neuron.2004.07.014

Chen, Z., B. Das, Y. Nakamura, D.A. DiGregorio, S.M. Young Jr., and M. Young. 2015. Ca^{2+} channel to synaptic vesicle distance accounts for the readily releasable pool kinetics at a functionally mature auditory synapse. *J. Neurosci.* 35:2083–2100. http://dx.doi.org/10.1523/JNEUROSCI.2753-14.2015

Cho, W., and R.V. Stahelin. 2006. Membrane binding and subcellular targeting of C2 domains. *Biochim. Biophys. Acta.* 1761:838–849. http://dx.doi.org/10.1016/j.bbalip.2006.06.014

Coppola, T., S. Magnin-Luthi, V. Perret-Menoud, S. Gattesco, G. Schiavo, and R. Regazzi. 2001. Direct interaction of the Rab3 effector RIM with Ca2+ channels, SNAP-25, and synaptotagmin. *J. Biol. Chem.* 276:32756–32762. http://dx.doi.org/10.1074/jbc.M100929200

Deng, L., P.S. Kaeser, W. Xu, and T.C. Südhof. 2011. RIM proteins activate vesicle priming by reversing autoinhibitory homodimerization of Munc13. *Neuron.* 69:317–331. http://dx.doi.org/10.1016/j.neuron.2011.01.005

Dick, O., S. tom Dieck, W.D. Altrock, J. Ammermüller, R. Weiler, C.C. Garner, E.D. Gundelfinger, and J.H. Brandstätter. 2003. The presynaptic active zone protein bassoon is essential for photoreceptor ribbon synapse formation in the retina. *Neuron.* 37:775–786. http://dx.doi.org/10.1016/S0896-6273(03)00086-2

Eggermann, E., I. Bucurenciu, S.P. Goswami, and P. Jonas. 2011. Nanodomain coupling between Ca^{2+} channels and sensors of exocytosis at fast mammalian synapses. *Nat. Rev. Neurosci.* 13:7–21. http://dx.doi.org/10.1038/nrn3125

Ehmann, N., S. van de Linde, A. Alon, D. Ljaschenko, X.Z. Keung, T. Holm, A. Rings, A. DiAntonio, S. Hallermann, U. Ashery, et al. 2014. Quantitative super-resolution imaging of Bruchpilot distinguishes active zone states. *Nat. Commun.* 5:4650. http://dx.doi.org/10.1038/ncomms5650

Fernández-Busnadiego, R., B. Zuber, U.E. Maurer, M. Cyrklaff, W. Baumeister, and V. Lučić. 2010. Quantitative analysis of the native presynaptic cytomatrix by cryoelectron tomography. *J. Cell Biol.* 188:145–156. http://dx.doi.org/10.1083/jcb.200908082

Fouquet, W., D. Owald, C. Wichmann, S. Mertel, H. Depner, M. Dyba, S. Hallermann, R.J. Kittel, S. Eimer, and S.J. Sigrist. 2009. Maturation of active zone assembly by *Drosophila* Bruchpilot. *J. Cell Biol.* 186:129–145. http://dx.doi.org/10.1083/jcb.200812150

Frank, C.A., M.J. Kennedy, C.P. Goold, K.W. Marek, and G.W. Davis. 2006. Mechanisms underlying the rapid induction and sustained expression of synaptic homeostasis. *Neuron.* 52:663–677. http://dx.doi.org/10.1016/j.neuron.2006.09.029

Frank, T., M.A. Rutherford, N. Strenzke, A. Neef, T. Pangršič, D. Khimich, A. Fejtová, E.D. Gundelfinger, M.C. Liberman, B. Harke, et al. 2010. Bassoon and the synaptic ribbon organize Ca2+ channels and vesicles to add release sites and promote refilling. *Neuron.* 68:724–738. http://dx.doi.org/10.1016/j.neuron.2010.10.027

Fujimoto, K., T. Shibasaki, N. Yokoi, Y. Kashima, M. Matsumoto, T. Sasaki, N. Tajima, T. Iwanaga, and S. Seino. 2002. Piccolo, a Ca2+ sensor in pancreatic beta-cells. Involvement of cAMP-GEFII.Rim2. Piccolo complex in cAMP-dependent exocytosis. *J. Biol. Chem.* 277:50497–50502. http://dx.doi.org/10.1074/jbc.M210146200

Gracheva, E.O., E.B. Maryon, M. Berthelot-Grosjean, and J.E. Richmond. 2010. Differential regulation of synaptic vesicle tethering and docking by UNC-18 and TOM-1. *Front. Synaptic Neurosci.* 2:141. http://dx.doi.org/10.3389/fnsyn.2010.00141

Graf, E.R., R.W. Daniels, R.W. Burgess, T.L. Schwarz, and A. DiAntonio. 2009. Rab3 dynamically controls protein composition at active zones. *Neuron.* 64:663–677. http://dx.doi.org/10.1016/j.neuron.2009.11.002

Graf, E.R., V. Valakh, C.M. Wright, C. Wu, Z. Liu, Y.Q. Zhang, and A. DiAntonio. 2012. RIM promotes calcium channel accumulation at active zones of the *Drosophila* neuromuscular junction. *J. Neurosci.* 32:16586–16596. http://dx.doi.org/10.1523/JNEUROSCI.0965-12.2012

Gratz, S.J., F.P. Ukken, C.D. Rubinstein, G. Thiede, L.K. Donohue, A.M. Cummings, and K.M. O'Connor-Giles. 2014. Highly specific and efficient CRISPR/Cas9-catalyzed homology-directed repair in *Drosophila*. *Genetics.* 196:961–971. http://dx.doi.org/10.1534/genetics.113.160713

Guerrero, G., D.F. Reiff, G. Agarwal, R.W. Ball, A. Borst, C.S. Goodman, and E.Y. Isacoff. 2005. Heterogeneity in synaptic transmission along a *Drosophila* larval motor axon. *Nat. Neurosci.* 8:1188–1196. http://dx.doi.org/10.1038/nn1526

Hallermann, S., and R.A. Silver. 2013. Sustaining rapid vesicular release at active zones: Potential roles for vesicle tethering. *Trends Neurosci.* 36:185–194. http://dx.doi.org/10.1016/j.tins.2012.10.001

Hallermann, S., A. Fejtová, H. Schmidt, A. Weyhersmüller, R.A. Silver, E.D. Gundelfinger, and J. Eilers. 2010a. Bassoon speeds vesicle reloading at a central excitatory synapse. *Neuron.* 68:710–723. http://dx.doi.org/10.1016/j.neuron.2010.10.026

Hallermann, S., M. Heckmann, and R.J. Kittel. 2010b. Mechanisms of short-term plasticity at neuromuscular active zones of *Drosophila*. *HFSP J.* 4:72–84. http://dx.doi.org/10.2976/1.3338710

Hallermann, S., R.J. Kittel, C. Wichmann, A. Weyhersmüller, W. Fouquet, S. Mertel, D. Owald, S. Eimer, H. Depner, M. Schwärzel, et al. 2010c. Naked dense bodies provoke depression. *J. Neurosci.* 30:14340–14345. http://dx.doi.org/10.1523/JNEUROSCI.2495-10.2010

Downloaded from http://rupress.org/jcb/article-pdf/216/1/231/1597608/jcb_201601098.pdf by guest on 08 February 2026

Harris, K.M., and J.K. Stevens. 1989. Dendritic spines of CA 1 pyramidal cells in the rat hippocampus: Serial electron microscopy with reference to their biophysical characteristics. *J. Neurosci.* 9:2982–2997.

Helmprobst, F., M. Frank, and C. Stigloher. 2015. Presynaptic architecture of the larval zebrafish neuromuscular junction. *J. Comp. Neurol.* 523:1984–1997. http://dx.doi.org/10.1002/cne.23775

Hibino, H., R. Pironkova, O. Onwumere, M. Vologodskaia, A.J. Hudspeth, and F. Lesage. 2002. RIM binding proteins (RBPs) couple Rab3-interacting molecules (RIMs) to voltage-gated Ca(2+) channels. *Neuron.* 34:411–423. http://dx.doi.org/10.1016/S0896-6273(02)00667-0

Holderith, N., A. Lorincz, G. Katona, B. Rózsa, A. Kulik, M. Watanabe, and Z. Nusser. 2012. Release probability of hippocampal glutamatergic terminals scales with the size of the active zone. *Nat. Neurosci.* 15:988–997. http://dx.doi.org/10.1038/nn.3137

Imig, C., S.-W. Min, S. Krinner, M. Arancillo, C. Rosenmund, T.C. Südhof, J. Rhee, N. Brose, and B.H. Cooper. 2014. The morphological and molecular nature of synaptic vesicle priming at presynaptic active zones. *Neuron.* 84:416–431. http://dx.doi.org/10.1016/j.neuron.2014.10.009

Ishiyama, S., H. Schmidt, B.H. Cooper, N. Brose, and J. Eilers. 2014. Munc13-3 superprimes synaptic vesicles at granule cell-to-basket cell synapses in the mouse cerebellum. *J. Neurosci.* 34:14687–14696. http://dx.doi.org/10.1523/JNEUROSCI.2060-14.2014

Jiao, W., S. Masich, O. Franzén, and O. Shupliakov. 2010. Two pools of vesicles associated with the presynaptic cytosolic projection in *Drosophila* neuromuscular junctions. *J. Struct. Biol.* 172:389–394. http://dx.doi.org/10.1016/j.jsb.2010.07.007

Kaeser, P.S., L. Deng, Y. Wang, I. Dulubova, X. Liu, J. Rizo, and T.C. Südhof. 2011. RIM proteins tether Ca^{2+} channels to presynaptic active zones via a direct PDZ-domain interaction. *Cell.* 144:282–295. http://dx.doi.org/10.1016/j.cell.2010.12.029

Kawasaki, F., S.C. Collins, and R.W. Ordway. 2002. Synaptic calcium-channel function in *Drosophila*: Analysis and transformation rescue of temperature-sensitive paralytic and lethal mutations of cacophony. *J. Neurosci.* 22:5856–5864.

Khimich, D., R. Nouvian, R. Pujol, S. Tom Dieck, A. Egner, E.D. Gundelfinger, and T. Moser. 2005. Hair cell synaptic ribbons are essential for synchronous auditory signalling. *Nature.* 434:889–894. http://dx.doi.org/10.1038/nature03418

Kittel, R.J., C. Wichmann, T.M. Rasse, W. Fouquet, M. Schmidt, A. Schmid, D.A. Wagh, C. Pawlu, R.R. Kellner, K.I. Willig, et al. 2006. Bruchpilot promotes active zone assembly, Ca2+ channel clustering, and vesicle release. *Science.* 312:1051–1054. http://dx.doi.org/10.1126/science.1126308

Koushika, S.P., J.E. Richmond, G. Hadwiger, R.M. Weimer, E.M. Jorgensen, and M.L. Nonet. 2001. A post-docking role for active zone protein Rim. *Nat. Neurosci.* 4:997–1005. http://dx.doi.org/10.1038/nn732

Kremer, J.R., D.N. Mastronarde, and J.R. McIntosh. 1996. Computer visualization of three-dimensional image data using IMOD. *J. Struct. Biol.* 116:71–76. http://dx.doi.org/10.1006/jsbi.1996.0013

Landis, D.M., A.K. Hall, L.A. Weinstein, and T.S. Reese. 1988. The organization of cytoplasm at the presynaptic active zone of a central nervous system synapse. *Neuron.* 1:201–209. http://dx.doi.org/10.1016/0896-6273(88)90140-7

Lee, J.S., W.-K. Ho, E. Neher, and S.-H. Lee. 2013. Superpriming of synaptic vesicles after their recruitment to the readily releasable pool. *Proc. Natl. Acad. Sci. USA.* 110:15079–15084. http://dx.doi.org/10.1073/pnas.1314427110

Leitinger, G., S. Masich, J. Neumüller, M.A. Pabst, M. Pavelka, F.C. Rind, O. Shupliakov, P.J. Simmons, and D. Kolb. 2012. Structural organization of the presynaptic density at identified synapses in the locust central nervous system. *J. Comp. Neurol.* 520:384–400. http://dx.doi.org/10.1002/cne.22744

Liu, K.S.Y., M. Siebert, S. Mertel, E. Knoche, S. Wegener, C. Wichmann, T. Matkovic, K. Muhammad, H. Depner, C. Mettke, et al. 2011. RIM-binding protein, a central part of the active zone, is essential for neurotransmitter release. *Science.* 334:1565–1569. http://dx.doi.org/10.1126/science.1212991

Mastronarde, D.N. 2005. Automated electron microscope tomography using robust prediction of specimen movements. *J. Struct. Biol.* 152:36–51. http://dx.doi.org/10.1016/j.jsb.2005.07.007

Matkovic, T., M. Siebert, E. Knoche, H. Depner, S. Mertel, D. Owald, M. Schmidt, U. Thomas, A. Sickmann, D. Kamin, et al. 2013. The Bruchpilot cytomatrix determines the size of the readily releasable pool of synaptic vesicles. *J. Cell Biol.* 202:667–683. http://dx.doi.org/10.1083/jcb.201301072

Matz, J., A. Gilyan, A. Kolar, T. McCarvill, and S.R. Krueger. 2010. Rapid structural alterations of the active zone lead to sustained changes in neurotransmitter release. *Proc. Natl. Acad. Sci. USA.* 107:8836–8841. http://dx.doi.org/10.1073/pnas.0906087107

McDonald, K.L., D.J. Sharp, and W. Rickoll. 2012. Transmission electron microscopy of thin sections of *Drosophila*: High-pressure freezing and freeze-substitution. *Cold Spring Harb. Protoc.* 2012:510–515. http://dx.doi.org/10.1101/pdb.prot068403

Melom, J.E., Y. Akbergenova, J.P. Gavornik, and J.T. Littleton. 2013. Spontaneous and evoked release are independently regulated at individual active zones. *J. Neurosci.* 33:17253–17263. http://dx.doi.org/10.1523/JNEUROSCI.3334-13.2013

Michel, K., J.A. Müller, A.-M. Oprişoreanu, and S. Schoch. 2015. The presynaptic active zone: A dynamic scaffold that regulates synaptic efficacy. *Exp. Cell Res.* 335:157–164. http://dx.doi.org/10.1016/j.yexcr.2015.02.011

Miśkiewicz, K., L.E. Jose, A. Bento-Abreu, M. Fislage, I. Taes, J. Kasprowicz, J. Swerts, S. Sigrist, W. Versées, W. Robberecht, and P. Verstreken. 2011. ELP3 controls active zone morphology by acetylating the ELKS family member Bruchpilot. *Neuron.* 72:776–788. http://dx.doi.org/10.1016/j.neuron.2011.10.010

Mittelstaedt, T., and S. Schoch. 2007. Structure and evolution of RIM-BP genes: Identification of a novel family member. *Gene.* 403:70–79. http://dx.doi.org/10.1016/j.gene.2007.08.004

Müller, M., K.S.Y. Liu, S.J. Sigrist, and G.W. Davis. 2012. RIM controls homeostatic plasticity through modulation of the readily-releasable vesicle pool. *J. Neurosci.* 32:16574–16585. http://dx.doi.org/10.1523/JNEUROSCI.0981-12.2012

Müller, M., Ö. Genç, and G.W. Davis. 2015. RIM-binding protein links synaptic homeostasis to the stabilization and replenishment of high release probability vesicles. *Neuron.* 85:1056–1069. http://dx.doi.org/10.1016/j.neuron.2015.01.024

Murthy, V.N., T.J. Sejnowski, and C.F. Stevens. 1997. Heterogeneous release properties of visualized individual hippocampal synapses. *Neuron.* 18:599–612. http://dx.doi.org/10.1016/S0896-6273(00)80301-3

Murthy, V.N., T. Schikorski, C.F. Stevens, and Y. Zhu. 2001. Inactivity produces increases in neurotransmitter release and synapse size. *Neuron.* 32:673–682. http://dx.doi.org/10.1016/S0896-6273(01)00500-1

Nakamura, Y., H. Harada, N. Kamasawa, K. Matsui, J.S. Rothman, R. Shigemoto, R.A. Silver, D.A. DiGregorio, and T. Takahashi. 2015. Nanoscale distribution of presynaptic Ca^{2+} channels and its impact on vesicular release during development. *Neuron.* 85:145–158. http://dx.doi.org/10.1016/j.neuron.2014.11.019

Neher, E. 2015. Merits and limitations of vesicle pool models in view of heterogeneous populations of synaptic vesicles. *Neuron.* 87:1131–1142. http://dx.doi.org/10.1016/j.neuron.2015.08.038

Peled, E.S., and E.Y. Isacoff. 2011. Optical quantal analysis of synaptic transmission in wild-type and rab3-mutant *Drosophila* motor axons. *Nat. Neurosci.* 14:519–526. http://dx.doi.org/10.1038/nn.2767

Petersen, S.A., R.D. Fetter, J.N. Noordermeer, C.S. Goodman, and A. DiAntonio. 1997. Genetic analysis of glutamate receptors in *Drosophila* reveals a retrograde signal regulating presynaptic transmitter release. *Neuron.* 19:1237–1248. http://dx.doi.org/10.1016/S0896-6273(00)80415-8

Reiff, D.F., P.R. Thiel, and C.M. Schuster. 2002. Differential regulation of active zone density during long-term strengthening of *Drosophila* neuromuscular junctions. *J. Neurosci.* 22:9399–9409.

Rizzoli, S.O., and W.J. Betz. 2005. Synaptic vesicle pools. *Nat. Rev. Neurosci.* 6:57–69. http://dx.doi.org/10.1038/nrn1583

Rosenmund, C., J.D. Clements, and G.L. Westbrook. 1993. Nonuniform probability of glutamate release at a hippocampal synapse. *Science.* 262:754–757. http://dx.doi.org/10.1126/science.7901909

Rostaing, P., R.M. Weimer, E.M. Jorgensen, A. Triller, and J.-L. Bessereau. 2004. Preservation of immunoreactivity and fine structure of adult *C. elegans* tissues using high-pressure freezing. *J. Histochem. Cytochem.* 52:1–12. http://dx.doi.org/10.1177/002215540405200101

Rostaing, P., E. Real, L. Siksou, J.-P. Lechaire, T. Boudier, T.M. Boeckers, F. Gertler, E.D. Gundelfinger, A. Triller, and S. Marty. 2006. Analysis of synaptic ultrastructure without fixative using high-pressure freezing and tomography. *Eur. J. Neurosci.* 24:3463–3474. http://dx.doi.org/10.1111/j.1460-9568.2006.05234.x

Sakaba, T., A. Stein, R. Jahn, and E. Neher. 2005. Distinct kinetic changes in neurotransmitter release after SNARE protein cleavage. *Science.* 309:491–494. http://dx.doi.org/10.1126/science.1112645

Schindelin, J., I. Arganda-Carreras, E. Frise, V. Kaynig, M. Longair, T. Pietzsch, S. Preibisch, C. Rueden, S. Saalfeld, B. Schmid, et al. 2012. Fiji: An open-source platform for biological-image analysis. *Nat. Methods.* 9:676–682. http://dx.doi.org/10.1038/nmeth.2019

Schlüter, O.M., J. Basu, T.C. Südhof, and C. Rosenmund. 2006. Rab3 superprimes synaptic vesicles for release: Implications for short-term synaptic plasticity. *J. Neurosci.* 26:1239–1246. http://dx.doi.org/10.1523/JNEUROSCI.3553-05.2006

Downloaded from http://rupress.org/jcb/article-pdf/216/1/231/1597608/jcb_201601098.pdf by guest on 08 February 2026

Schmidt, H., S. Brachtendorf, O. Arendt, S. Hallermann, S. Ishiyama, G. Bornschein, D. Gall, S.N. Schiffmann, M. Heckmann, and J. Eilers. 2013. Nanodomain coupling at an excitatory cortical synapse. *Curr. Biol.* 23:244–249. http://dx.doi.org/10.1016/j.cub.2012.12.007

Schneggenburger, R., A.C. Meyer, and E. Neher. 1999. Released fraction and total size of a pool of immediately available transmitter quanta at a calyx synapse. *Neuron.* 23:399–409. http://dx.doi.org/10.1016/S0896-6273(00)80789-8

Siksou, L., F. Varoqueaux, O. Pascual, A. Triller, N. Brose, and S. Marty. 2009. A common molecular basis for membrane docking and functional priming of synaptic vesicles. *Eur. J. Neurosci.* 30:49–56. http://dx.doi.org/10.1111/j.1460-9568.2009.06811.x

Smith, P.D., G.W. Liesegang, R.L. Berger, G. Czerlinski, and R.J. Podolsky. 1984. A stopped-flow investigation of calcium ion binding by ethylene glycol bis(beta-aminoethyl ether)-N,N′-tetraacetic acid. *Anal. Biochem.* 143:188–195. http://dx.doi.org/10.1016/0003-2697(84)90575-X

Stanley, E.F. 2015. Single calcium channel domain gating of synaptic vesicle fusion at fast synapses; analysis by graphic modeling. *Channels (Austin).* 9:324–333. http://dx.doi.org/10.1080/19336950.2015.1098793

Stewart, B.A., H.L. Atwood, J.J. Renger, J. Wang, and C.F. Wu. 1994. Improved stability of *Drosophila* larval neuromuscular preparations in haemolymph-like physiological solutions. *J. Comp. Physiol. A Neuroethol. Sens. Neural Behav. Physiol.* 175:179–191. http://dx.doi.org/10.1007/BF00215114

Stigloher, C., H. Zhan, M. Zhen, J. Richmond, and J.-L. Bessereau. 2011. The presynaptic dense projection of the *Caenorhabditis elegans* cholinergic neuromuscular junction localizes synaptic vesicles at the active zone through SYD-2/liprin and UNC-10/RIM-dependent interactions. *J. Neurosci.* 31:4388–4396. http://dx.doi.org/10.1523/JNEUROSCI.6164-10.2011

Südhof, T.C. 2012. The presynaptic active zone. *Neuron.* 75:11–25. http://dx.doi.org/10.1016/j.neuron.2012.06.012

Wadel, K., E. Neher, and T. Sakaba. 2007. The coupling between synaptic vesicles and Ca^{2+} channels determines fast neurotransmitter release. *Neuron.* 53:563–575. http://dx.doi.org/10.1016/j.neuron.2007.01.021

Wagh, D.A., T.M. Rasse, E. Asan, A. Hofbauer, I. Schwenkert, H. Dürrbeck, S. Buchner, M.-C. Dabauvalle, M. Schmidt, G. Qin, et al. 2006. Bruchpilot, a protein with homology to ELKS/CAST, is required for structural integrity and function of synaptic active zones in *Drosophila*. *Neuron.* 49:833–844. http://dx.doi.org/10.1016/j.neuron.2006.02.008

Wang, Y., and T.C. Südhof. 2003. Genomic definition of RIM proteins: Evolutionary amplification of a family of synaptic regulatory proteins. *Genomics.* 81:126–137. http://dx.doi.org/10.1016/S0888-7543(02)00024-1

Wang, X., B. Hu, A. Zieba, N.G. Neumann, M. Kasper-Sonnenberg, A. Honsbein, G. Hultqvist, T. Conze, W. Witt, C. Limbach, et al. 2009. A protein interaction node at the neurotransmitter release site: Domains of Aczonin/Piccolo, Bassoon, CAST, and rim converge on the N-terminal domain of Munc13-1. *J. Neurosci.* 29:12584–12596. http://dx.doi.org/10.1523/JNEUROSCI.1255-09.2009

Weber, A.M., F.K. Wong, A.R. Tufford, L.C. Schlichter, V. Matveev, and E.F. Stanley. 2010. N-type Ca^{2+} channels carry the largest current: Implications for nanodomains and transmitter release. *Nat. Neurosci.* 13:1348–1350. http://dx.doi.org/10.1038/nn.2657

Weyhersmüller, A., S. Hallermann, N. Wagner, and J. Eilers. 2011. Rapid active zone remodeling during synaptic plasticity. *J. Neurosci.* 31:6041–6052. http://dx.doi.org/10.1523/JNEUROSCI.6698-10.2011

Zhai, R.G., and H.J. Bellen. 2004. The architecture of the active zone in the presynaptic nerve terminal. *Physiology (Bethesda).* 19:262–270. http://dx.doi.org/10.1152/physiol.00014.2004

Zhan, H., J. Bruckner, Z. Zhang, and K. O'Connor-Giles. 2016. Three-dimensional imaging of *Drosophila* motor synapses reveals ultrastructural organizational patterns. *J. Neurogenet.* 30:237–246. http://dx.doi.org/10.1080/01677063.2016.1253693

Downloaded from http://rupress.org/jcb/article-pdf/216/1/231/1597608/jcb_201601098.pdf by guest on 08 February 2026